ORIGINAL ARTICLE

Omentin-1 drives cardiomyocyte cell cycle arrest and metabolic maturation by interacting with BMP7

Huijun Yang[1,2,3] · Shen Song[2] · Jiacheng Li[4] · Yandong Li[2] · Jie Feng[2] · Quan Sun[1,5] · Xueting Qiu[1,5] · Ziwei Chen[2] · Xue Bai[2] · Xinchang Liu[2] · Hong Lian[2] · Lihui Liu[2] · Yongping Bai[1,5] · Guogang Zhang[1,5] · Yu Nie[2,6,7]

Abstract

Mammalian cardiomyocytes (CMs) undergo maturation during postnatal heart development to meet the increased demands of growth. Here, we found that omentin-1, an adipokine, facilitates CM cell cycle arrest and metabolic maturation. Deletion of *omentin-1* causes mouse heart enlargement and dysfunction in adulthood and CM maturation retardation in juveniles, including delayed cell cycle arrest and reduced fatty acid oxidation. Through RNA sequencing, molecular docking analysis, and proximity ligation assays, we found that omentin-1 regulates CM maturation by interacting directly with bone morphogenetic protein 7 (BMP7). Omentin-1 prevents BMP7 from binding to activin type II receptor B (ActRIIB), subsequently decreasing the downstream pathways mothers against DPP homolog 1 (SMAD1)/Yes-associated protein (YAP) and p38 mitogen-activated protein kinase (p38 MAPK). In addition, omentin-1 is required and sufficient for the maturation of human embryonic stem cell-derived CMs. Together, our findings reveal that omentin-1 is a pro-maturation factor for CMs that is essential for postnatal heart development and cardiac function maintenance.

Keywords Omentin-1 · BMP7 · Cardiomyocyte · Cell cycle arrest · Cell metabolism · hES-CMs · Postnatal heart development

Introduction

The heart is the first organ to form during embryogenesis [1]. Heart growth during pregnancy involves the formation of four ventricular chambers, but fetal cardiomyocytes

---

Huijun Yang and Shen Song have contributed equally to this work.

✉ Yongping Bai
baiyongping@csu.edu.cn

✉ Guogang Zhang
zhangguogang@csu.edu.cn

✉ Yu Nie
nieyu@fuwaihospital.org

1 Department of Geriatric Medicine, Xiangya Hospital, Central South University, Changsha 410008, China

2 State Key Laboratory of Cardiovascular Disease, National Center for Cardiovascular Disease, Fuwai Hospital, Chinese Academy of Medical Sciences and Peking Union Medical College, 167 Street, Beilishi Road, Xicheng District, Beijing 100037, People's Republic of China

3 Department of Cardiovascular Medicine, The Eighth Affiliated Hospital, Sun Yat-sen University, Shenzhen 518033, China

4 Center for Reproductive Medicine, Department of Obstetrics and Gynecology, Peking University Third Hospital, Beijing 100191, China

5 Department of Geriatric Medicine, National Clinical Research Center for Geriatric Disorders, Xiangya Hospital, Central South University, 87 Street, Xiangya Road, Kaifu District, Changsha 410008, People's Republic of China

6 Shenzhen Key Laboratory of Cardiovascular Disease, Fuwai Hospital Chinese Academy of Medical Sciences, Shenzhen 518057, China

7 National Health Commission Key Laboratory of Cardiovascular Regenerative Medicine, Fuwai Central-China Hospital, Central China Branch of National Center for Cardiovascular Diseases, Zhengzhou 450046, China

(CMs) cannot efficiently meet the needs of hemodynamics and body growth after birth [2]. To adapt the rapid growth of the body, fetal CMs undergo a dramatic transition to develop into adult CMs in a process termed CM maturation [3, 4]. CMs acquire unique features during maturation after birth, including a state of cell cycle arrest [5–8], a large rod-like shape [9], well-organized sarcomeres [10], and metabolism based on fatty acid oxidation [11–13]. A disruption in CM maturation during postnatal heart development could lead to structural heart diseases [14], cardiomyopathy [15], and even heart failure [16]. A number of regulators involved in CM maturation have been identified [12, 17–21], such as serum response factor [22], Meis1/Hoxb13 [23, 24], thyroid hormone[25, 26], estrogen-related receptor signaling [21] and agrin [27], but other factors that participate in CM maturation remain unclear.

Adipokines, which are synthesized and secreted by adipocytes, include dozens of molecules, such as omentin-1, leptin, adiponectin, apelin, resistin, glycolipids, tumor necrosis factor, interleukin-6, and visfatin [28]. Most adipokines are deleterious in cardiovascular diseases, except omentin-1, leptin, adiponectin and apelin, which are considered cardioprotective and participate in postnatal heart development and heart function maintenance [29]. *Apelin*-knockout (KO) mice display reduced cardiac contractility during postnatal heart development and suffer from heart failure within six months [30]. In pressure-overloaded conditions, adiponectin deficiency leads to progressive cardiac remodeling and diastolic heart failure [31]. Cardiac-specific deletion of the leptin receptor can lead to heart failure, which worsens under ischemic conditions [32, 33].

Omentin-1, as a newly identified adipokine, also known as intelectin-1, has been demonstrated that its expression is significantly decreased in patients with heart failure, and its downregulation is associated with a higher risk of adverse cardiac events during clinical follow-up [34–36]. In addition, experimental studies have shown that omentin-1 exerts cardioprotective effects under cardiac pathological conditions in mice. For instance, administration of omentin-1 protects the mice against cardiac remodeling following transverse aortic constriction through reductions in CM hypertrophy and fibrosis [37]. Omentin-1 can also improve cardiac function after myocardial ischemia–reperfusion injury by inhibiting CM apoptosis [38]. Nevertheless, the mechanisms by which omentin-1 maintains cardiac function are still unclear.

Recently, it was reported that the expression of *omentin-1* increases from the neonatal period to adulthood in both human and rhesus macaque hearts after birth [39]. Here, we generated an *omentin-1* knockout (*omentin-1$^{-/-}$*) mouse line and found that omentin-1 deficiency led to heart enlargement and dysfunction in adulthood and CM immaturity in juveniles. Hence, we hypothesized that omentin-1 is essential for cardiac maturation during postnatal heart development.

By employing RNA sequencing (RNA-seq) and functional studies, we demonstrated that omentin-1 promoted CM cell cycle arrest and metabolic maturation during postnatal heart development. Ingenuity Pathway Analysis (IPA) based on RNA-seq data revealed that bone morphogenic protein 7 (BMP7) might be a targeted regulator of omentin-1 during postnatal heart development. A molecular docking and simulation study showed that omentin-1 interacted with BMP7 and prevented it from binding to its receptor, activin type II receptor B (ActRIIB), as well as blocking two downstream pathways, SMAD1/YAP and p38 MAPK. Furthermore, we found that omentin-1 was required and sufficient for the maturation of human embryonic stem cell-derived CMs (hES-CMs). Thus, our studies uncover the role of omentin-1 as a regulator of CM cell cycle arrest and metabolic maturation in postnatal heart development and hES-CMs, providing new insight into the role of omentin-1 in cardiac function.

Materials and methods

The data, methods, and materials that support the results of this study are available upon reasonable request from the corresponding author, Yu Nie (nieyu@fuwaihospital.org).

Mice

Global *omentin-1* knockout (*omentin-1$^{-/-}$*) mice were a gift presented by Prof. Hui Xie at Central South University (Changsha, China). The generation method of *omentin-1$^{-/-}$* mice has been described in a previous study [40]. Briefly, TALEN technology was used to generate the global *omentin-1$^{-/-}$* mice by Cyagen Biosciences Inc. (Guangzhou, China). One base (A) was inserted into the exon 4 of the mouse *omentin-1* gene in one strand, resulting in a frameshift mutation and depletion of omentin-1 protein. TALEN mRNAs were microinjected into fertilized eggs obtained by superovulation of female C57BL/6 mice mating with the males of the same strain, and the mice were genotyped by PCR and DNA sequencing analysis with the forward primer 5′-CTGCACAGAGGAAGACTGTGGACC-3′ and the reverse primer 5′-AAAGGTGTTGTAGTTGGC CCAGTTG-3′. The positive founders were selected to breed, and the *omentin-1$^{-/-}$* mice were produced. Compared to their wild-type (WT) littermates, *omentin-1$^{-/-}$* mice were almost normal with regard to basic body parameters, functional parameters of the liver and kidneys, and serum levels of glucose, insulin, and iron, and there were no significant differences in their lifespan and body weight (Supplementary Fig. 1a). All the animal protocols were approved by the Institutional Animal Care and Use Committee (IACUC), Fuwai Hospital, Chinese Academy of Medical Sciences.

Echocardiography

Cardiac function was detected using echocardiography (Visual Sonics, Vevo 2100, USA; 40 MHz 550/770 probe) [41, 42]. Before the operation, the left-sided chest fur of the mice was depilated. Postnatal day 7 (P7) and P14 mice were conscious and unsedated, while P30 and P90 mice were mildly sedated via inhalation of 1.0–2.5% isoflurane mixed with medical-grade oxygen via a nose cone. The heart rate of each mouse was at least 450 beats per minute (bpm), and parasternal long-axis and short-axis views were obtained by M-mode imaging. The electronic caliper in the accompanying Visual Sonics Vevo Imaging software was used to calculate the parameters of ejection fraction (EF), fractional shortening (FS), left ventricular anterior-wall thickness (LVAW), left ventricular posterior-wall thickness (LVPW), left ventricular end-diastolic dimension (LVEDD), and left ventricular end-systolic dimension (LVESD). Three to five contraction cycles were selected for analysis, and these indexes were automatically averaged and analyzed by software for each mouse. All echocardiography measurements were performed in a blinded manner.

Magnetic resonance imaging (MRI)

Before MRI scanning, the mice were anesthetized with inhalation of 1.0–2.5% isoflurane mixed with oxygen via a gas anesthesia machine (Matrx VML, 29,089, USA). When the mouse was sedated, it was fixed on the scanning bed in the prone position, with the heart centered on a coil of the aligned array. The respiration and electrocardiogram (ECG) of mice were monitored in real time according to physiological parameters (SA Instruments, Belgium). All MRI acquisitions were gated using both respiration and ECG triggering. Hot air was used to keep the animal's body temperature at 37 ± 1 °C.

Heart function was detected by a 7.0 T/160 mm small animal magnetic resonance scanner (Varian, Palo Alto, USA). The gradient echo sequence was first used to scan the standard horizontal-axis position of the mouse chest axis, and a cardiac cine scan was performed. The two-chamber view of the left ventricle was obtained in the standard horizontal-axis image through a positioning line of the left ventricular apex and the mitral valve midpoint. Then, the four-chamber heart view was obtained from the two-chamber plane through the same positioning line. On the two-chamber or four-chamber cardiac plane of the left ventricle, a series of left ventricle short-axis cross-sectional images were obtained through the positioning line from the heart bottom to the apex perpendicular to the long axis of the left ventricle. At the end of exhalation, the scan started from the apex and progressed to the bottom of the heart. Seven to eight slices of left ventricle short-axis cross-sectional images with 1-mm thickness

and no gap between slices were obtained. The cine scanning parameters were as follows: time of echo (TE): 3 ms, time of repetition (TR): 173.41 ms, flip angle (flip angle): 20, layer thickness (thickness): 1 mm, interlayer distance (Gap): 0 mm, field of view (FOV): 50.2×50.4 mm, excitation number (NEX): 2, matrix (matrix): 128×128, cine frame: 12. In every heartbeat cycle, 12 movie frame images were collected. These results obtained by cardiac cine were used to observe heart morphology and wall thickness at the spatial level.

Adult CM isolation

The Langendorff method for isolation of CMs from adult mouse hearts and the perfusion buffer collocation method were used as previously described [25, 43–45]. Studies have shown that estrogen has an important effect on the maturation of CMs [21]. To exclude interference of estrogen, we used male mice for our experiments. WT and *omentin-1$^{-/-}$* male mice (12–14 weeks) were anesthetized with pentobarbital sodium (100 mg/kg) by intraperitoneal injection. The heart was quickly removed from the chest and retrogradely perfused with 37 °C perfusion solution for 3 min followed by enzyme solution for approximately 20–30 min. The enzyme solution consisted of collagenase type 2 (0.5 mg/ml; Worthington Biochemical, LS004176, USA), collagenase type 4 (0.5 mg/ml; Worthington Biochemical, LS004188, USA), protease type XIV (0.02 mg/ml; Sigma, P5147, USA), and 0.5 mg/ml bovine serum albumin (BSA, Sigma, SRE0096, USA) in perfusion solution. When the heart was swollen and pale and the boundaries of the left and right ventricles were not clear, the heart was considered digested. Then, the digested heart was transferred into a dish full of fresh stop buffer (perfusion solution containing 5% BSA), and the atria, right ventricle, and atrioventricular junction area were cut away, leaving only the left ventricle. Using eye scissors and fine forceps, the left ventricle was minced into small pieces (~ 1 mm), and the dissociated CMs were harvested and filtered through a 100-μm mesh. The sample was centrifuged at $50 \times g$ for 60 s; the supernatant was discarded; and the pellet was resuspended in gradient Ca^{2+} solutions containing 125, 250, and 500 mM Ca^{2+} every 15 min. After CM Ca^{2+} restoration, the contraction ability of CMs was immediately detected with an IonOptix system.

CM contractility measurement

Sarcomere shortening was recorded using the IonOptix system (Myocyte Calcium & Contractility Recording System, HMSYS, IonOpix, USA). First, CMs were loaded into the recording chamber. After 5 min of deposition, they were perfused with normal Tyrode solution at a rate of 1.5 ml/min. Then, pace CMs were stimulated with a 1 Hz field

using a MyoPacer field stimulator (8 V, 4 ms) for 5 min, and healthy CMs (rod shape, sharp edge, clear cross-striations, and no spontaneous contraction) were selected for recording. Then, the selected CM were moved into the center of the field of view and lined up horizontally, and the focus of the microscope was adjusted until sarcomere striations were clearly visible. In our study, we used the sarcomere length recording task to record CM shortening and relengthening. The sarcomere length changes (15–20 stable contractions) were recorded under field stimulation. Once the contractility traces were acquired, the data were analyzed with the IonWizard software following the instructions.

RNA-seq and bioinformatics analysis

Total RNA of WT and *omentin-1*$^{-/-}$ mice heart samples across four developmental stages (P7, P14, P30, and P90) and total RNA of primary rat CMs (PBS, BMP7, and BMP7 + omentin-1) were extracted with an RNAeasy mini kit (Qiagen, 74,106, Germany). All groups had 3 replicates. The quantity of total RNA was measured with a NanoDrop 2000 (Thermo Fisher Scientific, USA), and the quality was detected with an Agilent Bioanalyzer 2100 (Agilent Technologies, USA). In total, 3 µg of total RNA with an RIN value no less than 8.0 for each sample was considered acceptable for library preparation. The RNA libraries were prepared using TruSeq library preparation kits (Illumina, RS-122–2001, USA) following the manufacturer's protocols and sequenced on an Illumina NovaSeq 6000 sequencing platform by Novogene Bioinformatics Technology Co., Ltd. (Beijing, China). The raw RNA reads were generated using standard protocols, and quality control determination was performed. The RNA-seq reads were mapped to the GRCm38 mouse reference genome or the Rnor_6.0 assembly using STAR (version 2.5.1b) with the default parameters, and the uniquely mapped reads were counted by featureCounts (https://github.com/topics/featurecounts). DESeq2 was used to perform statistical analysis of differential gene expression. Hierarchical clustering was performed with Euclidean distance as the metric. Differentially expressed genes (DEGs) were determined as those with a fold-change > 2 and an FDR *P* value < 0.05. All sequencing data related to this work have been deposited in the National Center of Biotechnology Information database (accession number PRJNA681365).

Weighted correlation network analysis (WGCNA) was performed with the R package WGCNA, which is a useful method to identify the phenotype-related gene modules and key modules that contribute to developmental traits. All WT and *omentin-1*$^{-/-}$ mice samples from P7 to P90 were used to construct the coexpression network. We then chose a soft thresholding power β to calculate adjacencies in the individual sets and turned the adjacencies into a topological overlap matrix (TOM). Topological overlap is a robust and biologically meaningful method to measure the strength of coexpression relationship of two genes with respect to all other genes in the network. Genes with highly similar coexpression relationships were grouped together by performing average linkage hierarchical clustering on the topological overlap. The modules were identified as branches (clusters) cutting from the hierarchical clustering tree that was calculated by a dynamic tree cut algorithm. To merge modules whose expression profiles were very similar, we calculated the module eigengenes (MEs) and clustered them on their consensus correlations. Modules with highly correlated eigengenes were merged, and the correlation coefficient *r* and the correlation-adjusted *p* value were used to calculate module-trait relationships. Key modules were identified using the following criteria: $r > 0.7$ and adjusted *p* value < 0.005. The biological meaning of the key module was identified by Gene Ontology (GO) enrichment analysis in Metascape (https://metascape.org). The Kolmogorov–Smirnov (KS) test was used to calculate *p* values of density plots. The KS test can assess if any two independent distributions are similar or different by generating cumulative probability plots for the two distributions. A lower probability is associated with a lower likelihood that two distributions are similar. Conversely, a higher value or a value closer to 1 is associated with greater similarity of the two distributions. The density plots were generated using R.

Mitochondrial respiration of heart tissue

Through high-resolution respirometry, mitochondrial functional parameters, including oxidative capacity and efficiency, were directly assessed. The oxygen consumption rate was measured in fresh heart homogenates using an Oxygraph-2 k (Oroboros Instruments, Innsbruck, Austria). Using a manual grinder, we homogenized the hearts in Mir05 buffer (2 ml tissue homogenizer). Fatty acid oxidative capacity was determined in the presence of malate (2.0 mmol/L), octanoyl-carnitine (50 mol/L), and ADP (1.0 mmol/L), and then the citrate cycle-derived substrates glutamate (10.0 mmol/L) and succinate (10.0 mmol/L) subsequently added to measure maximal oxidative capacity. State 3 was defined as the state with the ability to oxidize mitochondrial substrates. We assessed the maximum uncoupled respiratory capacity of the electron transport chain (state u) via incremental titrations with carbonyl cyanide m-chlorophenyl hydrazone (CCCP) (0.1 mmol/L per step). In the presence of oligomycin, the respiratory response due to proton leak and not coupled to adenosine triphosphate (ATP) synthesis was measured (state 4o). Using the state 3/state 4o and state 4o/state u respiration ratios, the respiratory control ratio and leak control ratio were calculated as markers of mitochondrial coupling and proton leak.

Tissue mitochondrial extraction and measurement of oxidative phosphorylation (OXPHOS) proteins

According to the manufacturer's instructions, mitochondria were extracted from heart tissue using a mitochondrial extraction kit (tissues) (Lot: C3606, Beyotime, China). To evaluate the enzyme activity of the mitochondrial OXPHOS complex, Western blots of the OXPHOS proteins in the electron transport chain complexes were performed using an anti-total OXPHOS primary antibody cocktail (458,099, Invitrogen, 1:20,000) containing antibodies against the CI subunit NDUFB8, the CII subunit succinate dehydrogenase subunit B (SDHB), the CIII subunit cytochrome b-c1 complex subunit 2 core protein 2 (UQCRC2), the CIV subunit cytochrome c oxidase subunit 1 I and CV alpha subunit (MTCO1) and the Complex IV subunit ATP synthase subunit alpha of Complex V (ATP5A). The quantified OXPHOS proteins were explored by band intensity assessment using ImageJ (https://imagej.en.softonic.com/), and the data were normalized to the total protein load.

Quantification of mitochondrial DNA

Using a DNA extraction kit (D3396-02 tissue DNA kit, Omega, USA), genomic/mitochondrial DNA was extracted from the heart tissues of P30 mice. Mitochondrial content can be determined directly via SYBR green analysis using purified DNA (Applied Biosystems, 4,309,155, USA). In this regard, the levels of NADH dehydrogenase subunit 1 (mt-Nd1), encoded by mitochondrial DNA, were normalized to the levels of lipoprotein lipase (Lpl), encoded by genomic DNA. The primers were as follows: mt-Ndl, forward primer 5′-TCCGAGCATCTTATCCACGC-3′, reverse primer 5′-GTATGGTGGTACTCCCGCTg-3′;

Lpl, forward primer 5′-GGAGAAGCCATCCGTGTG AT-3′, reverse primer 5′-CTCAGGCAGAGCCCTTTC TC-3′.

CM counting

Cardiomyocyte counting was performed on P14 WT and *omentin-1*$^{-/-}$ mice hearts as described previously [23]. Fresh hearts were harvested and immediately fixed in 4% PFA for 2–3 h. Afterward, the samples were treated with collagenase D (2.4 mg/mL, Roche, 11,088,858,001) and B (1.8 mg/mL, Roche, 11,088,807,001) for 12 h at 37 °C. Then, isolated CMs were obtained by spinning down the supernatant ($50 \times g$ for 1 min), and the heart was minced into smaller pieces. This procedure was repeated until no more CMs were dissociated from the tissue. Isolated CMs were suspended in 5 mL PBS, and cell counting was conducted using a hemocytometer. We performed at least three counts per sample, and every count was calculated for a 10 µL suspension of CMs. The number of CMs ranged from 55 to 90 per count, and approximately 500–800 CMs were counted in one group.

Primary CM culture

Hearts were harvested from 1-day-old neonatal Sprague–Dawley rats. A Neonatal Heart Dissociation Kit (Miltenyi Biotech, Teterow, 130–098-373, Germany) and a gentleMACS™ Octo Dissociator (Miltenyi Biotech, Teterow, 130–093-235, Germany) were used to isolate CMs [46]. The tissue lysate was then filtered through a 100-µm cell strainer, and the cells were centrifuged for 5 min at 1000 rpm. After isolation, CMs were allowed to attach and recover over 24 h in DMEM supplemented with 10% FBS at 37 °C with 5% CO_2. Then CMs were treated daily with recombinant human omentin-1 protein (300 ng/mL, R&D System, 9137-IN-050, USA) or recombinant human BMP7 protein (100 ng/mL, R&D System, 354-BP-010/CF, USA) for 2 consecutive days. In YAP or P38 MAPK inhibitor interference assays, CMs were pretreated with YAP inhibitor verteporfin (1 µg/mL, MCE, HY-B0146) or the p38 MAPK inhibitor SB203580 (10 µM, MCE, HY-10256A) 1 h before BMP7 treatment. After treatment, CMs were harvested for assays and immunofluorescence staining.

EdU incorporation assay, cell cycle progression assay, JC-1 assay, and apoptosis assays

An EdU incorporation assay was performed by using a Click-iT™ Plus EdU Alexa Fluor™ 647 Flow Cytometry Assay Kit (Thermo Fisher Scientific, C10634, USA). Cultured primary CMs were incubated with DMSO or 10 µM EdU for 24 h. Following the instructions and standard procedures CMs were fixed and permeabilized, stained with the intracellular anti-α-actinin (sarcomeric) antibodies conjugated with PE (Meltenyi Biotec, 130–106-937, Germany), detected with Click-iT™ EdU, and analyzed by flow cytometry in a FACSAria Flow Cytometer (BD Biosciences, USA).

Cell cycle progression was detected using PI/RNase Staining Buffer (BD Biosciences, 550,825, USA). Following the manufacturer's instructions, in brief, harvested CMs were fixed and permeabilized with 70% to 80% ethanol at -20 °C overnight. For staining, 1×10^6 cells per test were resuspended in 0.5 mL of PI/RNase Staining Buffer. The cells were incubated for 15 min at room temperature and analyzed on a flow cytometer (Accuri C6 plus Cytometer, BD Biosciences, USA) within 1 h.

JC-1 assay detection was performed following the JC-1 assay kit instructions (Beyotime, C2006, China). After CMs were stained, analysis was performed in a FACSAria Flow Cytometer (BD Biosciences, USA).
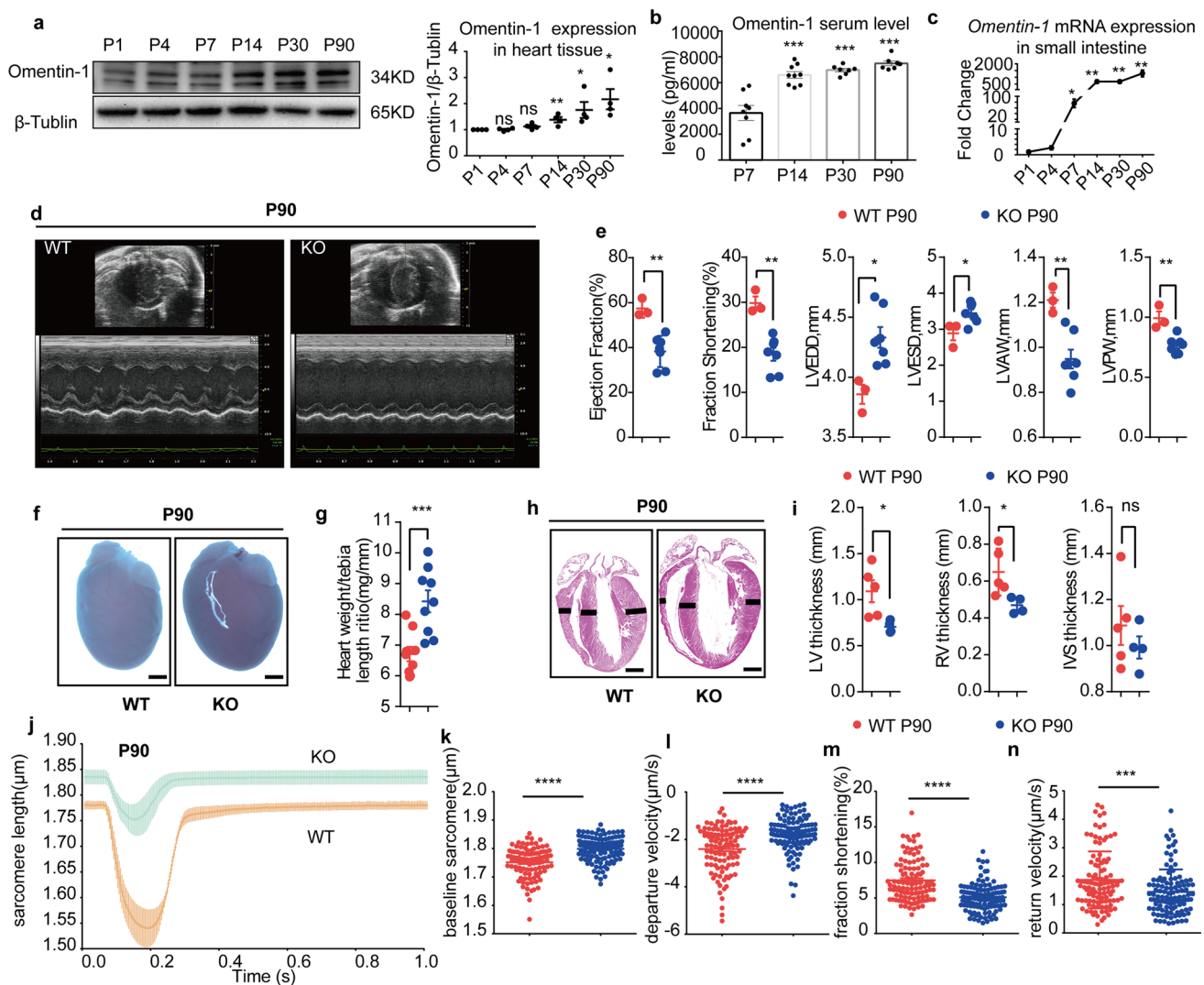
Fig. 1 Omentin-1 deficiency leads to heart enlargement and dysfunction in adulthood. **a** Western blot analysis of omentin-1 expression in mouse heart tissue during postnatal heart development (from postnatal day 1 (P1) to P90). The expression levels were normalized to those of P1. **b** ELISA detected the serum levels of omentin-1 at P7, P14, P30, and P90. **c** Real-time quantitative PCR (RT−qPCR) analysis of the messenger RNA (mRNA) expression of *omentin-1* in mouse small intestinal tissue. **d** Representative echocardiography images of wild-type and *omentin-1* knockout (*omentin-1$^{-/-}$*) mice hearts at P90. KO, *omentin-1$^{-/-}$* mice; WT, wild-type mice. **e** Statistical analysis showing decreased ejection fraction (EF), decreased fractional shortening (FS), increased left ventricle end-diastolic and end-systolic dimensions (LVEDD and LVESD), and reduced left ventricular anterior and posterior wall thickness (LVAW and LVPW) in *omentin-1$^{-/-}$* mice

hearts. **f** Representative whole-heart images of WT and *omentin-1$^{-/-}$* mice. **g** Heart weight/tibia length (HW/TL) ratios in WT and *omentin-1$^{-/-}$* mice. **h** Representative hematoxylin–eosin (HE) staining of WT and *omentin-1$^{-/-}$* mice hearts. **i** HE staining showing enlarged hearts with reduced wall thickness in *omentin-1$^{-/-}$* mice; scale bar, 1 mm. **j–n** Average sarcomere shortening waveform (**j**) shown as the mean ± SEM. Orange trace: 104 cardiomyocytes (CMs) from 4 WT mice. Green trace: 113 CMs from 4 *omentin-1$^{-/-}$* mice. CMs are stimulated at 1 Hz. *omentin-1$^{-/-}$* mice CMs increased the baseline sarcomere length (**k**) decreased the departure velocity (**l**), reduced the FS (**m**), and slowed the return velocity (**n**). The data are presented as the mean ± SEM. ****$p < 0.0001$, ***$p < 0.001$, **$p < 0.01$, *$p < 0.05$ by unpaired Student's *t* test

Apoptosis assays were detected by using PE Annexin V (BD Biosciences, 560,930, USA). According to the manufacturer's instructions, CMs were stained and analyzed by flow cytometry in a FACSAria Flow Cytometer (BD Biosciences, USA).

Enzyme-linked immunosorbent assay (ELISA)

Serum levels of omentin-1 were quantitated using commercially available ELISA kits following the manufacturer's instructions (Lifespan Bioscience, LS-F28511, USA). These kits were specifically designed for mouse omentin-1 detection, and the detection range was 50–100 pg/ml. Serum

samples of P7, P14, P30, and P90 were diluted tenfold and tested in duplicate in the same plate. Standard curves were plotted with the absorbance of each standard on the x-axis and the concentration on the y-axis, and the concentrations of the samples were calculated.

Co-immunoprecipitation (Co-IP) assay

A Co-IP assay was performed for the omentin-1 and BMP7 proteins. CMs that were transduced with omentin-1-flag lentivirus for 48 h were lysed in a buffer containing RIPA (Thermo Fisher Scientific Cat: 89,900) and phenylmethylsulfonyl fluoride (PMSF) (Beyotime Cat: ST506 1:100). The CM lysates were subjected to Co-IP with anti-FLAG antibody beads (FLAG Immunoprecipitation Kit, Cat: FLA-GIPT1) or anti-BMP7 antibody with protein G (Cell Signaling Technology Cat: 70024 s) beads followed by Western blot. The Co-IP assay for smad1 and YAP was similar except that antibody against SMAD1 (Abclonal, A1101) and YAP (CST, 14074S) were used.

IPA

IPA upstream regulator analysis (version 01–13, Ingenuity Systems, Redwood City, CA, USA; www. ingenuity.com) was used to identify key regulatory molecules predicted to explain the gene expression differences observed between WT and *omentin-1$^{-/-}$* mice. The common upstream regulators of major maturation stages P14 and P30 were obtained by overlapping.

Proximity ligation assay (PLA)

A PLA (Duolink, no. DUO92101, Sigma) was performed following the manufacturer's instructions. Primary rat CMs were isolated and plated on cell culture confocal glass (Millicell EZ slide). Briefly, cells were fixed with 4% paraformaldehyde and then blocked with Duolink® Blocking Solution. The cells were incubated with primary anti-BMP7 (1:100, Proteintech, 12,221–1-AP) and anti-ActRIIB (1:100, Santa Cruz, sc-376593) antibodies overnight at 4 ℃. The cells were analyzed with a ZEISS LSM800 confocal laser scanning microscope.

Molecular docking

To analyze the interaction of omentin-1, BMP7, and ActRIIB, the X-ray structures of complex BMP7 binding with ActRIIB and omentin-1 protein binding were retrieved from the research collaboratory structural bioinformatics (RCSB) protein database. After the quality and integrity of omentin-1, BMP7, and ActRIIB were validated, BMP7 was set as a receptor, and omentin-1 and ActRIIB were docked to BMP7 with HEX DOCK. The sampling method used a 15-angstrom receptor box, 3D Fourier transform (FFT) was performed, and shape and charge (shape and electro) correction methods were used. Other default parameters were conserved, and the maximum binding energy of the docking result was retained. Based on the stable binding conformation, a virtual box was added, and the minimum distance from the box edge to the protein was 1 nm. To neutralize the system, TIP3 water molecules and other ions were added. In a 30 ns simulation, the models of BMP7, BMP7−ActRIIB, and BMP7−omentin-1 were equilibrated. Molecular dynamics simulation was completed with YASARA V14 software. The other parameters were the defaults except that the Amber99sb force field was used, the PME method was used, and the cutoff was set as 12.

To ensure the correctness of the docking model, we compared the BMP7 and ActRIIB docking model and the crystal structure of the BMP7−ActRIIB interaction complex using PyMol v1.7. The RMS was 1.04 and the docked model was almost superimposed on the crystal structure (Supplementary Fig. 7a), suggesting that the parameter model used in this study was rational.

Nuclear/cytoplasmic fraction isolation

For cell nuclear/cytoplasmic fraction isolation, an NE-PER™ Nuclear and Cytoplasmic Extraction Reagents kit (Thermo Fisher Scientific, 78,833, USA) was used to separate CM nuclei and cytoplasm. Briefly, cells were harvested, washed with PBS and centrifuged at $500 \times g$ for 5 min. Then the supernatant was carefully removed and discarded, and the cell pellet was left to dry as completely as possible. Ice-cold CER I was added to the cell pellet, and cytoplasmic and nuclear protein extraction was performed following the manufacturer's instructions.

Human ESC-H9 cell culture and cardiomyocyte differentiation

Human ESC-H9 cells were cultured on feeder-free Matrigel (Corning, CC160, USA) and fed daily with PSCeasy hESC/iPSC modified essential 8 medium (Cellapy, CA1014500, China). The cells were routinely passaged every 3–4 days (d) at 80–90% confluence, using 0.5 mM ethylenediaminetetraacetic acid (EDTA) (Cellapy, CA3001500, China) in PBS without $MgCl_2$ or $CaCl_2$ (Gibco, 14,190,144, USA). The cells were cultured at 37 °C with 5% CO_2 in a humidified incubator (Thermo Fisher Scientific, Waltham, USA). The hESC-H9 cells were differentiated into CMs using a small molecule-based monolayer cardiac differentiation method as described previously [47]. Briefly, cells were cultured
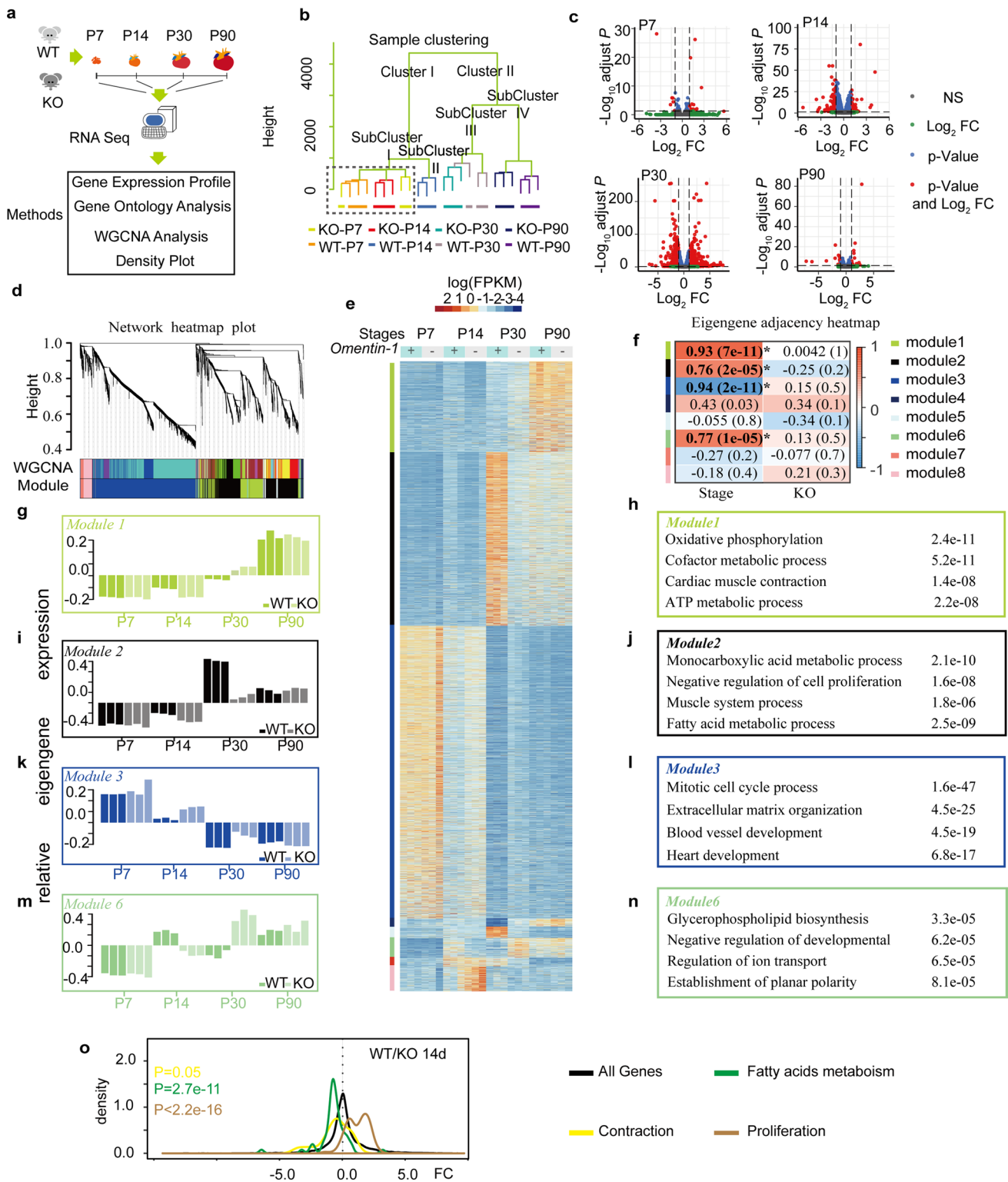
in basal CDM3 medium (CDM3, consisting of RPMI 1640 (Life Technologies, 11,875, USA), 500 μg/mL *O. sativa*-derived recombinant human albumin (Sigma-Aldrich, A0237, USA), and 213 μg/mL L-ascorbic acid 2-phosphate (Sigma-Aldrich, 49,752, USA) supplemented with 6 μM CHIR99021 (a GSK-3 inhibitor, Selleck Chemicals, S1263, USA) from d0-d2. On d2, the medium was changed to CDM3 supplemented with 2 μM Wnt-C59 (a Wnt inhibitor, Selleck Chemicals, S7037, USA). Beginning on d4, the medium was changed to fresh basal CDM3 medium every

◄**Fig. 2** RNA-sequencing (RNA-seq) analysis reveals that the *omentin-1⁻/⁻* heart has distinct transcriptional behaviors during development. **a** Experimental scheme of RNA-seq analysis of wild-type and *omentin-1⁻/⁻* mice hearts from different developmental stages (postnatal day 7 (P7), P14, P30, and P90) and analysis of the gene expression profiles, biological functions (Gene Ontology pathways), and key events during development (WGCNA and density plot). KO, *omentin-1⁻/⁻* mice; WT, wild-type mice. **b** Hierarchical clustering of significantly regulated genes; *omentin-1⁻/⁻* mice samples at P14 are clustered together with WT P7 samples instead of WT P14 samples. **c** Differentially expressed gene (DEG) analysis between WT and *omentin-1⁻/⁻* mice showed that transcriptome divergence mainly occurs at P14 and P30. There were 22 DEGs at P7, 299 DEGs at P14, 1270 DEGs at P30, and 39 DEGs at P90. **d** WGCNA dendrograms of WT and *omentin-1⁻/⁻* mice hearts revealing different expression modules. The branches in the hierarchical clustering dendrograms correspond to modules. Color-coded module membership is displayed in the color bars below the dendrograms. **e** Heatmaps of gene expression profiles clustered by WGCNA. Eight modules were identified in total and are labeled accordingly. **f** Four modules were obtained, including modules 1, 2, 3, and 6. The gradient variance of color from blue to red represented the connectivity of eigengenes in the different modules from weak to strong. The module-stage correlation cutoff values were $r \geq 0.7$ and $p \leq 0.005$ (*r*, Pearson's correlation coefficient). **g–n** The eigengene expression of modules and top Gene Ontology (GO) terms enriched in corresponding modules are listed with their *P* values. **g**, **h** represent Module 1, **i**, **j** represent Module 2, **k**, **l** represent Module 3, and **m**, **n** represent Module 6. **o** Density plots with the fold change (FC) expression values of genes from four representative categories for *omentin-1⁻/⁻* mice hearts relative to WT hearts. The X-axis indicates the log2 (FC) in gene expression. The black line indicates the expression of all genes. The colored lines toward the left and right sides of the black line indicate downregulation and upregulation of pathways, respectively

other day. On d9-d12, beating CMs began to appear after differentiation was initiated. On d12-d16, ESC-CMs were purified with glucose-depleted culture medium containing abundant lactate (Cellapy, CA2005100, China) as previously described [48].

Flow cytometry

After hES-CM differentiation and purification, CMs were dissociated with CardioEasy CM dissociation buffers I and II (Cellapy, CA2011100 and CA2012100, China). Then, the cells were fixed and permeated with an Inside Stain Kit (Miltenyi Biotec, 130–090-477, Germany) and stained with anti-α-actinin (Sarcomeric) antibodies conjugated with PE (Miltenyi Biotec, 130–106-937, USA) or REA Control (I)-PE (Miltenyi Biotec, 130–104-613, USA) following the manufacturer's instructions. Briefly, cells were washed three times with PBS, fixed with Inside Fix buffer for 20 min at room temperature, and incubated for 30 min with staining antibodies diluted in Inside Permeabilization buffer. Then, the cells were washed with PBS and analyzed with an FAC-SAria™ III Flow Cytometer (BD Biosciences, USA). Data were collected from at least 90,000 events.

## CardioExcyte 96 (CE96) function analysis

Function analysis was performed with CE96 (Nanion Technologies, Munich, Germany), a system for CM impedance measurements. Before seeding cells, multiple cell-populated CE96 sensor plates were coated with fibronectin (Sigma Aldrich, F0895, USA) for 2 hours (h) inside the incubator (37 °C, 5.0% CO_2). Cell was seeded at a density of approximately 50,000 cells per well, and the cells were not touched or moved for 48 h. After this time, a medium change was performed every 2 to 3 d for approximately 1 week. The impedance signal increased after seeding, and when a monolayer of CMs was stably formed, the impedance of CMs plateaued, at which time the experiment was started. In this experiment, several indexes (base impedance, amplitude, beat rate) were recorded at the start of the experiment (baseline) and after *omentin-1* knockdown (KD) or overexpression (OE) for 14 d. Data were analyzed using the automated online analysis (OA) feature of the software CardioExcyte.

Lentivirus transduction

For the virus transduction experiments, *omentin-1* mRNA was knocked down in hES-CMs by infection with Lv:CMV:siRNA-*omentin-1* at a multiplicity of infection (MOI) of 300 or overexpressed by infection with Lv:CMV:*omentin-1* at an MOI of 300. Control cells were infected by equivalent Lv:CMV:Null (GeneChem, Shanghai, China). The virus was diluted in DMEM in the presence of hexadimethrine bromide (Polybrene, 4 µg/ml). *Omentin-1* KD vector, OE vector, and empty viral vector (EV) were transduced into CMs on day 16 of the differentiation protocol. Fourteen days after transduction, at day 30, all functional and structural parameters of CMs were examined. The *omentin-1*-OE vector was also used in primary CMs and transduced at least 48 h before experiments.

Seahorse XF24 extracellular analyzer

Primary CMs or hES-CMs were seeded onto a Matrigel-coated XF24 Cell Culture Microplate (Seahorse Bioscience, 102,343–100, USA) at 6×10^4 cells/well [49]. Following the manufacturer's instructions, an XF24 Extracellular Flux Analyzer (Seahorse Bioscience, Agilent, USA) was used to measure the oxygen consumption rate (OCR) in a Mito Stress Test assay (Seahorse Bioscience, 103,015–100, USA) or extracellular acidification rate (ECAR) in a glucose stress assay (Seahorse Bioscience, 103,020–100, USA). The OCRs were estimated before and after the sequential addition of 1 mM oligomycin, 1 mM FCCP, and 0.75 mM rotenone/myxothiazol. Mitochondrial respiration capacity was determined according to the OCRs, including the basal OCR and the OCRs in response to oligomycin (an ATP synthase
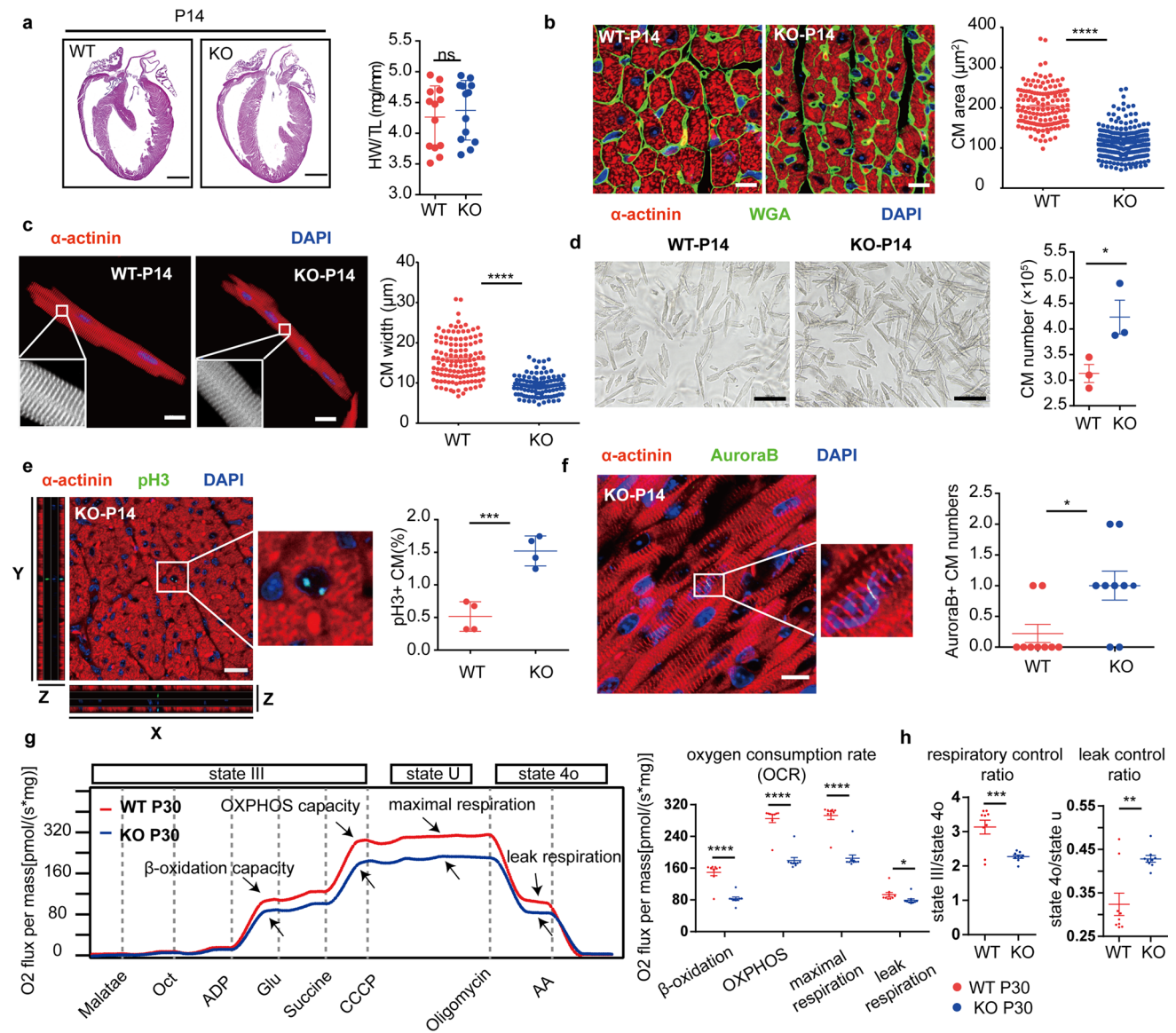
Fig. 3 Cardiomyocyte (CM) cell cycle arrest is delayed and metabolism immature in juveniles following *omentin-1* deletion. **a** Hematoxylin–eosin (HE) staining and heart weight (HW)/tibia length (TL) ratios of wild-type (WT) and *omentin-1*$^{-/-}$ mice hearts at postnatal day 14 (P14) ($n = 10$–13 per group). KO, *omentin-1*$^{-/-}$ mice; WT, wild-type mice. **b** Wheat germ agglutinin (WGA) staining showing that the CM cross-sectional area is smaller in *omentin-1*$^{-/-}$ mice hearts, scale bar, 10 μm. The quantitative analyses represent the counts in multiple fields from three independent samples per group (~30 cells per field, total ~150–200 cells per group). **c** Isolated CMs at P14 showing that the width of CMs is smaller and that the CMs exhibited more disordered arrangement sarcomeric structures; scale bar, 20 μm. **d** Representative images of isolated CMs and quantification of the total number of CMs. Approximately 5×10^2–8×10^2 CMs in each group were counted with a hemocytometer. Each point

in the boxplots represents the total number of CMs isolated from a single sample from one mouse. Each group contained three independent samples, and we averaged three different counts per sample. **e** Evaluation of CM mitotic activity by assessment of pH3$^+$ CMs in P14 heart sections. A representative image of *omentin-1*$^{-/-}$ mice obtained by confocal microscopy is shown; scale bar, 20 μm. The percentage of pH3$^+$ CMs per heart section was analyzed by high-content analysis. **f** Quantification analysis of cytokinesis (Aurora B kinase) in CMs in P14 heart sections. A representative image of *omentin-1*$^{-/-}$ mice is shown; scale bar, 10 μm. **g** Mitochondrial oxidative capacity in the hearts of WT and *omentin-1*$^{-/-}$ mice at P30. **h** Mitochondrial respiratory control ratio and the leak control ratio in WT and *omentin-1*$^{-/-}$ mice hearts. The data are presented as the mean ± SEM. ****$p < 0.0001$, ***$p < 0.001$, **$p < 0.01$, *$p < 0.05$ by unpaired Student's t test

inhibitor), FCCP (carbonyl cyanide 4-(trifluoromethoxy) phenylhydrazone, a mitochondrial uncoupler), and rotenone (a complex I inhibitor). The ECAR was tested in XF medium

under basal conditions. Subsequently, glucose (10 mM), oligomycin (1 μM), and 2-DG (50 mM) were loaded in XF assay medium, and the ECARs were determined in response

to glucose and 2-DG in order to represent glycolysis and glycolytic capacity respectively. The OCRs and ECARs were normalized to the cell protein level.

Histology

Harvested hearts were fixed in 4% paraformaldehyde at room temperature for 24–48 h. Then, the sections were dehydrated in an ethanol and xylene series and paraffin-embedded. The *omentin-1$^{-/-}$* and WT mice hearts were sliced in a four-chamber view. Four sections were collected for each heart. Hematoxylin–eosin (HE) and Masson's trichrome staining was performed using standard procedures [50].

Immunofluorescence

For immunofluorescence staining, we chose paraffin-embedded sections. The procedure included deparaffinization in xylene and rehydration through graded ethanol. Antigen retrieval was performed with an EDTA solution in a high-temperature high-pressure manner. The sections were permeabilized with 0.3% Triton X-100, and nonspecific background staining was blocked with 10% goat serum (ZSGB-Bio, ZLI-9056, China). The sections were incubated with primary antibodies overnight at 4 °C. After 12–16 h of incubation, the slides were washed in PBS three times and then incubated with secondary antibodies for 45 min at 37 °C. The slides were again washed in a dark room and then stained with DAPI (Sigma, D9542) for 15 min to label the nuclei. For CM immunofluorescence staining, CMs were cultured in confocal dishes (Millicell EZ Slide, 4 well glass, PEZGS0416); after treatment, the cells were fixed with 4% paraformaldehyde for 15 min and washed with PBS 3 times. Then, the procedures described above were performed, including blocking of nonspecific background staining and incubation with primary antibody/secondary antibodies. The primary antibodies included anti-cTnT (rabbit monoclonal, Abcam, ab8295, UK), anti-phosphorylated histone H3 (pH3) (rabbit monoclonal, Millipore, 06–507, USA), anti-α-actinin (mouse monoclonal, Abcam, ab9465, UK), anti-Aurora-B (rabbit monoclonal, Sigma, A5102, USA), anti-caveolin-3 (rabbit monoclonal, Abcam, ab173575, USA), anti-α-SMA (rabbit monoclonal, Abcam, ab242395, USA), anti-Ki67 (rabbit monoclonal, Abcam, ab1667, China), anti-Tom20 (rabbit monoclonal, abclonal, A19403, China), anti-omentin-1 (rabbit polyclonal, Gentex, GTX32687, USA), and anti-tropomyosin (sarcomeric) (mouse monoclonal, Sigma, T9283, USA).

The secondary antibodies were conjugated to Alexa Fluor 488 (donkey anti-rabbit, Invitrogen, A-21206, USA) and Alexa Fluor 594 (donkey anti-mouse, Invitrogen, A32744, USA). For wheat germ agglutinin (WGA) staining, the slides were deparaffinized, rinsed three times in PBS, directly incubated with a primary antibody against WGA conjugated to FITC (Abcam, ab20528) for 1 h at room temperature, and then washed three times. Fluorescence was observed under a ZEISS LSM800 confocal laser scanning microscope. To quantify the positive cells of the heart, at least three independent hearts per group with three different views and positions were captured at 20× or 40× magnification. The cell area, cell perimeter, and Aurora B$^+$ CMs were all quantified per high-power field (HPF) by the ImageJ.

High-content analysis

The percentage of pH3$^+$ CMs per section at P14 and the percentage of pH3$^+$ primary CMs after omentin-1 treatment were analyzed by high-content analysis (ImageXpress Micro, Molecular Devices, Sunnyvale, CA). Images were first acquired following the instructions. The marker-controlled watershed segmentation algorithm was used, with nuclei treated as internal markers. Nuclei were assigned as objects (1×) and then overlaid with the pH3-488 or α-actinin-594 channel. Nuclei that were fully enclosed within the pH3-488 area were deemed pH3$^+$ nuclei (1×3). A nucleus completely wrapped by the 594 channel was considered to belong to an α-actinin$^+$ CM (1×2). CMs were classified as pH3$^+$ if pH3$^+$ nuclei overlapped with α-actinin$^+$ CMs (1×2×3). The percentage was calculated by dividing the number of pH3$^+$ nuclei overlapping with α-actinin$^+$ CMs (1×2×3) by the number of α-actinin$^+$ CMs (1×2).

Extraction of heart extracellular matrix (ECM)

The extraction of heart ECM was performed as previously described [27]. Hearts from P1, P4, P7, P14, P30, and P90 C57 mice were collected, embedded in optimal cutting temperature (O.C.T) compound (Sakura, 2615–00, USA) and frozen at -80 °C. Then, the hearts were cut into 100-µm fragments and immersed in 2% Triton X-100 and 20 mM EDTA solution overnight at room temperature. The matrices were washed with PBS, and an ultrasonic cell-crushing device was used for ECM disruption (amplitude 25%, 5 sonications pulse, 5 s pause, duration at least 5 min until a uniform transparent liquid was obtained).

Western blot analysis

Western blotting was performed as previously described [6, 49]. Briefly, hearts or CM samples were harvested, homogenized and then incubated in RIPA lysis buffer with 1 mM PMSF (Beyotime Institute of Biotechnology, ST505, Beijing, China). A total of 30 µg of protein was loaded onto an SDS-PAGE gel, and the separated proteins were subsequently blotted onto a nitrocellulose membrane. The membranes were blocked with 5% fetal calf serum (FCS) in PBS
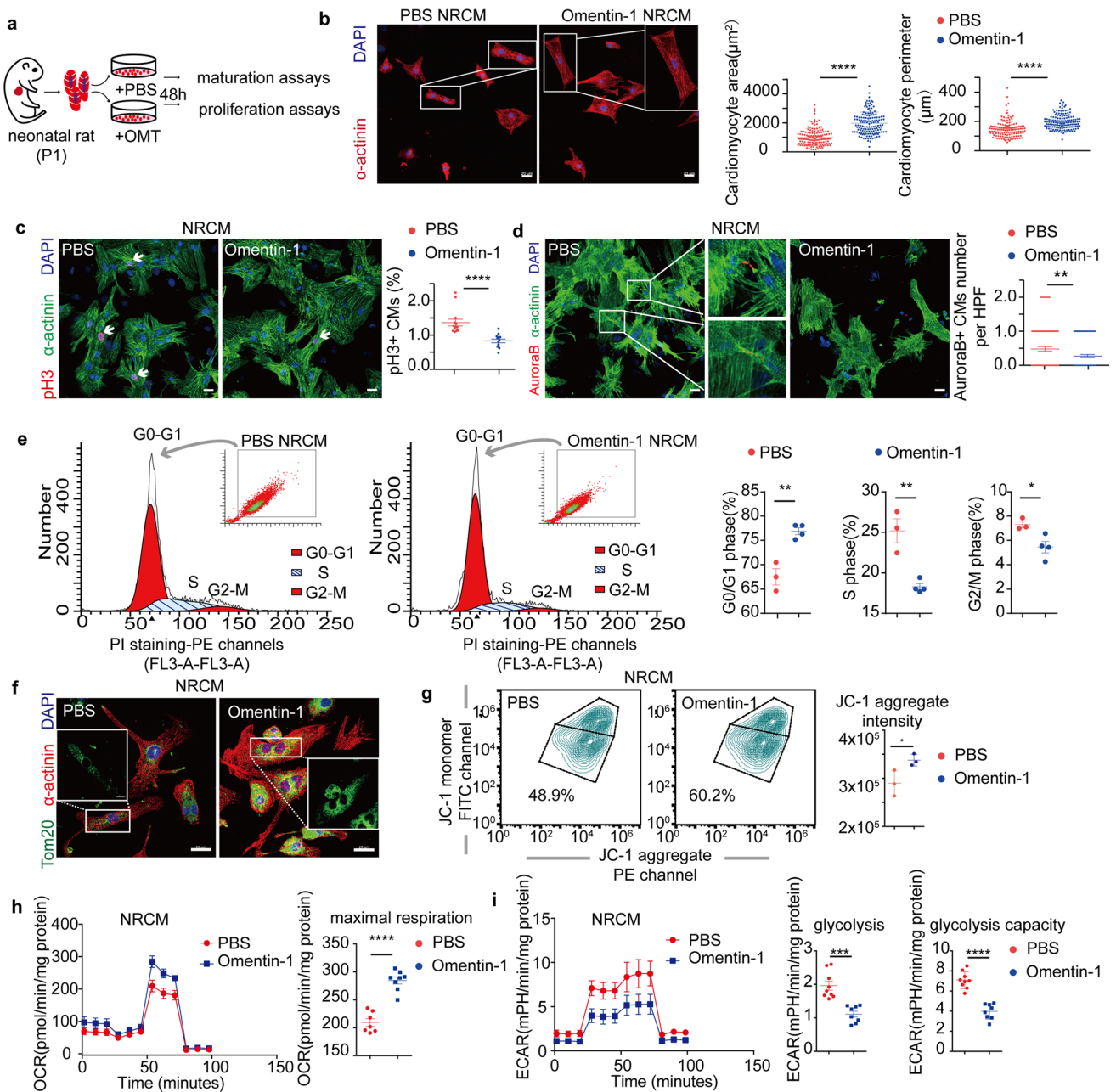
at room temperature for 1 h and then incubated overnight at 4 °C with the following primary antibodies: anti-Omentin-1 (GeneTex, GTX32687, 1:1000 dilution), anti-CDK2, anti-CDK4, anti-CDK6, anti-cyclin D1 (CST, all 1:1000, Cell Cycle Regulation Antibody Sampler Kit #9932), anti-c-Myc (CST, 18,583, 1:1000 dilution), anti-BMP7 (Proteintech, 12,221–1-AP, 1:1000 dilution), anti-Flag (Sigma, SAB1306078, 1:1000 dilution), anti-YAP (CST, 14,074, 1:1000 dilution), anti-YAP-s127 (CST, 4911, 1:1000 dilution), anti-phospho-Smad1-S206 rabbit (Abclonal, AP0295, 1:1000 dilution), anti-SMAD1 (Abclonal, A1101, 1:1000 dilution), anti-phospho-p38 MAPK-T180/Y182 rabbit (Abclonal, AP0526, 1:1000 dilution), and anti-p38 MAPK

(Abclonal, A14401, 1:1000 dilution). On the following day, the membranes were washed with TBST three times and then incubated with secondary antibodies at room temperature for 1 h. The signals were detected by employing an enhanced chemiluminescence (ECL) kit (GE Healthcare). Protein quantification was performed using ImageJ, and the level of each protein was normalized to that of the internal control protein or to the total protein level.

Real-time quantitative PCR (qRT-PCR)

To assess gene expression, total RNA was extracted from samples using TRIzol reagent (Invitrogen, 10,296,028).

◀**Fig. 4** Omentin-1 is a regulator of cardiomyocyte (CM) quiescence and metabolic maturation. **a** Experimental plan to evaluate the effects of omentin-1 on the proliferation and maturation of primary neonatal rat CMs (NRCM). **b** Representative image of omentin-1-treated CMs (left); scale bar, 20 μm. Quantification of the area and perimeter of α-actinin$^+$ CMs (right). Three independent samples including 130–140 CMs were obtained by confocal microscopy and measured by ImageJ. **c** Representative image of pH3$^+$ CMs, scale bar, 20 μm. Quantification of pH3$^+$ α-actinin$^+$ neonatal CMs after 48 h of omentin-1 treatment as evaluated by high-content analysis. **d** Representative image of Aurora B$^+$ CMs; scale bar, 20 μm. Quantification of the number of Aurora B$^+$ α-actinin$^+$ CMs per high-power field (HPF) by confocal microscopy. **e** Representative image of cell cycle progression as detected by flow cytometry. The initial and last red peaks represent the G0-G1 and G2-M stages, respectively, and the middle is the S stage. Compared to those of untreated CM, the percentages of omentin-1-treated CMs in G0-G1 phase and S/G2-M phase were higher and lower, respectively. **f** Omentin-1 treatment increases mitochondrial Tom20 expression and distribution. A representative image of Tom20$^+$ CMs is shown; scale bar, 20 μm. **g** Flow cytometry analyses of JC-1. Omentin-1-treated CMs exhibited more mitochondrial activity (JC-1 aggregates). Representative profile (left) and JC-1 aggregate intensity quantitation (right). **h** Mito Stress Test assays reflecting oxygen consumption rate (OCR) profiles in response to oligomycin (an ATP synthase inhibitor), carbonyl cyanide p-trifluoromethoxyphenylhydrazone (FCCP, an uncoupler of electron transport and OXPHOS), and rotenone and antimycin (electron transport chain blockers). Representative profile of omentin-1-treated CMs (left) and quantification of maximal respiration capacity (right). **i** A glycolytic stress assay was performed following glucose, oligomycin and 2-DG treatments. The extracellular acidification rate (ECAR) profile (left) shows that omentin-1 treatment decreased glycolysis and glycolytic capacity (right). The data are presented as the mean ± SEM. ****$p < 0.0001$, ***$p < 0.001$, **$p < 0.01$, *$p < 0.05$ by unpaired Student's t test

Then, PrimeScript RT Master Mix (Takara, RR036A) was used to convert RNA to cDNA. qRT-PCR was performed using SYBR Green qPCR Master Mix (Applied Biosystems, 4,309,155, USA) in triplicate, and amplification was achieved on a Vii7 Real-Time PCR System (Thermo Fisher Scientific, Waltham, USA). All primers for the reactions are listed in Supplementary Table 1.

Quantification, unification and statistical analysis

All data are presented as the mean ± standard error of the mean (SEM). Unpaired Student's t test was used to assess significant differences between two groups. A value of $p < 0.05$ was considered to indicate statistical significance.

Results

Omentin-1 deletion induces cardiac enlargement and dysfunction

To explore whether omentin-1 is involved in postnatal heart development, we examined *omentin-1* expression at different developmental stages. Western blot analysis demonstrated that omentin-1 protein level in heart tissue was upregulated in the early juvenile (P14), later juvenile (P30), and adulthood (P90) stages compared with that at the neonatal stage (P1) (Fig. 1a and Supplementary Fig. 1b). In mice, cardiac omentin-1 was recruited from serum and synthesized by the intestine (Supplementary Fig. 1c). ELISA revealed that serum omentin-1 was elevated at P14, P30, and P90 (Fig. 1c). Consistent with the expression profiles in the heart and serum, RT-qPCR confirmed that *omentin-1* messengerRNA (mRNA) expression was dynamically increased in the mouse small intestine during postnatal development (Fig. 1b).

To evaluate the role of omentin-1 in the heart, we generated an *omentin-1* knockout (*omentin-1$^{-/-}$*) mouse line and performed a cardiac phenotypic assessment. Western blot analysis showed that omentin-1 was effectively deleted in *omentin-1$^{-/-}$* mice (Supplementary Fig. 1d). Echocardiography revealed that the heart function of *omentin-1$^{-/-}$* mice gradually decreased from the juvenile (P14) to adulthood (P90) (Supplementary Fig. 2a and Supplementary Table 2). Cardiac dysfunction with heart enlargement appeared in *omentin-1$^{-/-}$* mice at P90 (Fig. 1d-f, Supplementary Fig. 2b, Movie S1). We also found that the heart weight/tibia length ratio (HW/TL) of *omentin-1$^{-/-}$* mice was markedly larger at P90 than that of WT mice (Fig. 1g). Hematoxylin–eosin (HE) staining showed that the *omentin-1$^{-/-}$* mice heart became enlarged (Fig. 1h-i).

To assess cardiac contractility at the cellular level, CMs were isolated, and the IonOptix system was used to measure CM contractility by sarcomere shortening. The contraction waveforms (Fig. 1j) demonstrated that P90 *omentin-1$^{-/-}$* mice CMs had significantly greater resting sarcomere lengths (Fig. 1k), slower contraction velocities (Fig. 1l), smaller contraction amplitudes (Fig. 1m), and slower relaxation velocities (Fig. 1n), suggesting that omentin-1 deficiency disturbs CM contractibility. Together, these results demonstrate that *omentin-1* deletion causes progressive heart enlargement and dysfunction in mice with abnormal CM contraction, indicating that omentin-1 is essential for postnatal heart development.

Omentin-1 participates in postnatal heart development

To explore the mechanisms of omentin-1 involvement in heart function, we compared the heart transcriptomes between *omentin-1$^{-/-}$* and WT mice at P7, P14, P30, and P90 (Fig. 2a). Unsupervised hierarchical clustering analysis revealed that *omentin-1$^{-/-}$* mice at P14 were transcriptionally related to WT mcie at P7 rather than at P14, suggesting a relative retardation in postnatal cardiac development in the
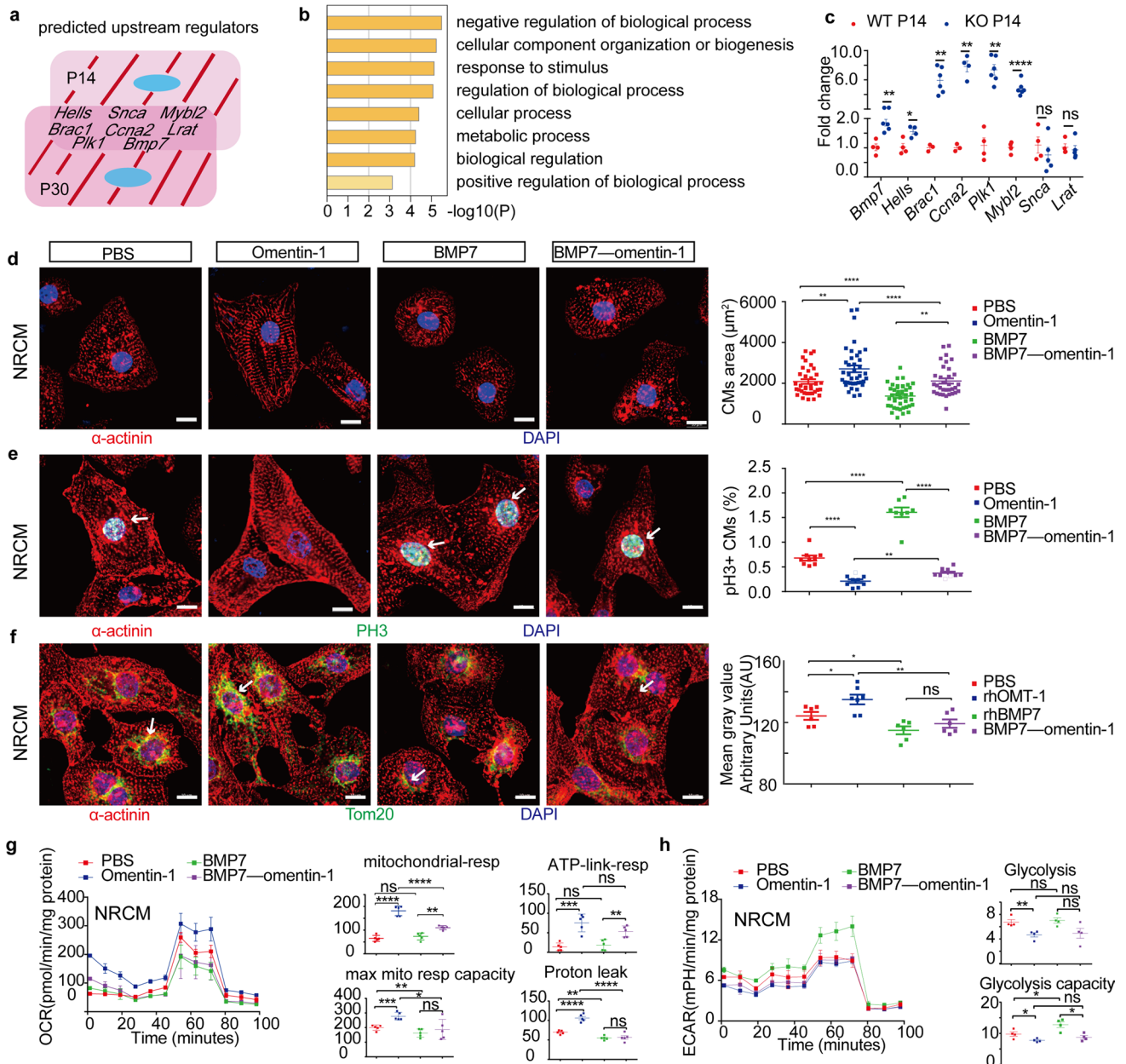
Fig. 5 Omentin-1 controls cardiomyocyte (CM) proliferation and metabolic maturation by blocking BMP7. **a**, **b** The Venn diagram in **a** illustrates eight common genes between two major maturation stages (postnatal day 14 (P14) and P30), which were predicted by the upstream regulator tool in Ingenuity Pathway Analysis for the differentially expressed genes (DEGs). The eight upstream regulators are shown (*Bmp7*, *Hells*, *Brac1*, *Ccna2*, *Plk1*, *Mybl2*, *Snca*, and *Lart*). **b** These molecules were enriched in metabolic and other cellular processes based on Metascape analysis. **c** Real-time quantitative PCR (RT−qPCR) showing that *Bmp7*, *Hells*, *Brac1*, *Ccna2*, *Plk1*, and *Mybl2* were significantly upregulated, while SNCA and LART were not changed, in P14 *omentin-1⁻/⁻* mice hearts. **d**–**f** Immunostaining of α-actinin, DAPI, pH3 and Tom20 in four different treatment groups. The four groups included 1) a group of CMs treated with PBS (con-

trol), 2) a group of CMs treated with human recombinant omentin-1 (300 ng/ml), 3) a group of CMs treated with human recombinant BMP7 (100 ng/ml), and 4) a group of CMs cotreated with omentin-1 and BMP7 for 48 h. **d** α-actinin and DAPI immunostaining were used to characterize the CM cell areas (scale bar, 10 μm). **e** pH3 immunostaining was used to characterize CM proliferation (scale bar, 20 μm). **f** Tom20 immunostaining was used to characterize the CM mitochondrial distribution (scale bar, 20 μm). **g**, **h** The results of a mitochondrial stress assay **g** and glycolysis stress assay **h** demonstrated the mitochondrial respiration, ATP-linked respiration, proton leak, glycolysis, and glycolysis capacity in PBS-treated (control), omentin-1-treated, BMP7-treated, or BMP7–omentin-1-cotreated CMs. The data are presented as the mean ± SEM. ****$p < 0.0001$, ***$p < 0.001$, **$p < 0.01$, *$p < 0.05$ by unpaired Student's *t* test
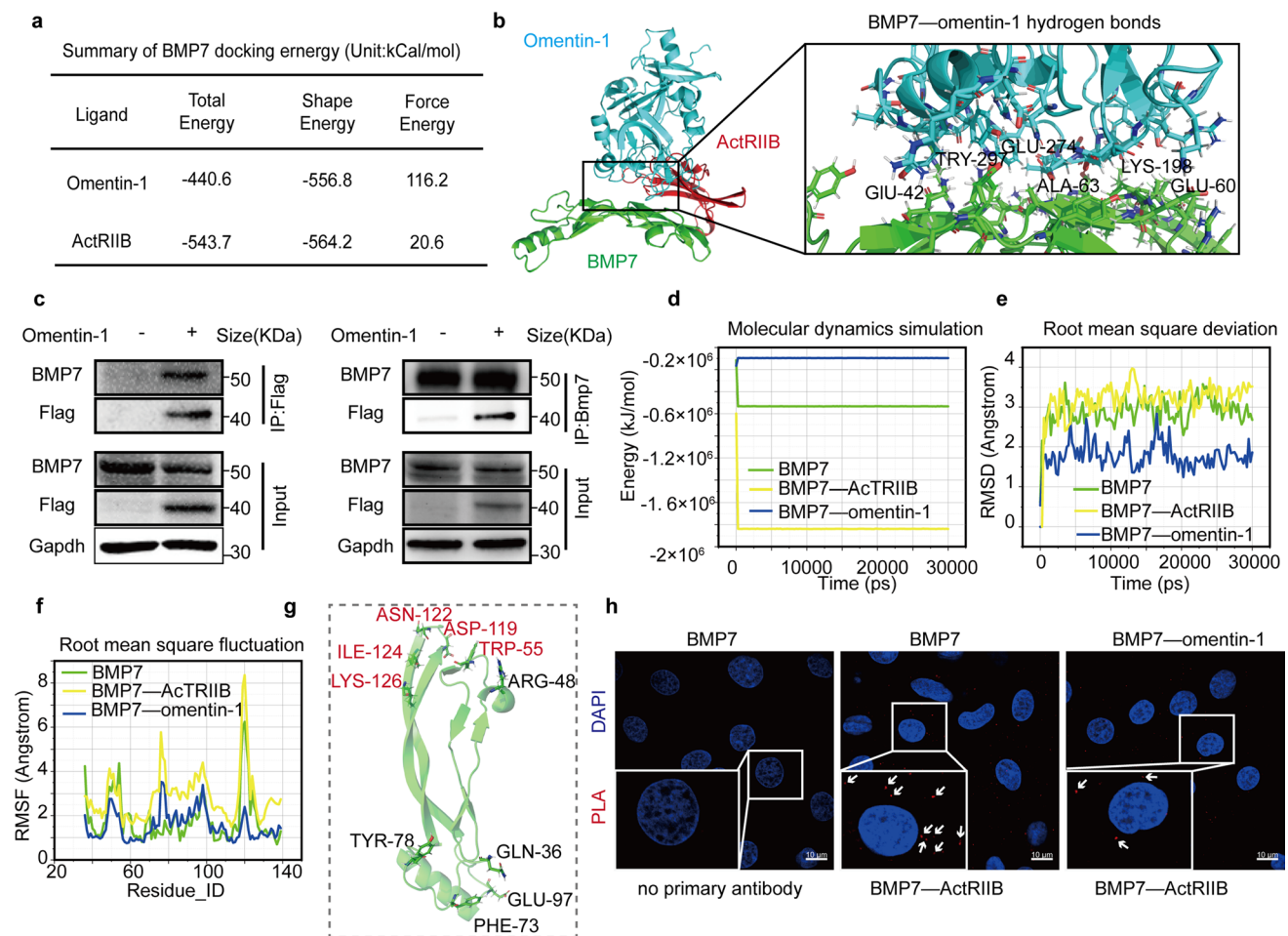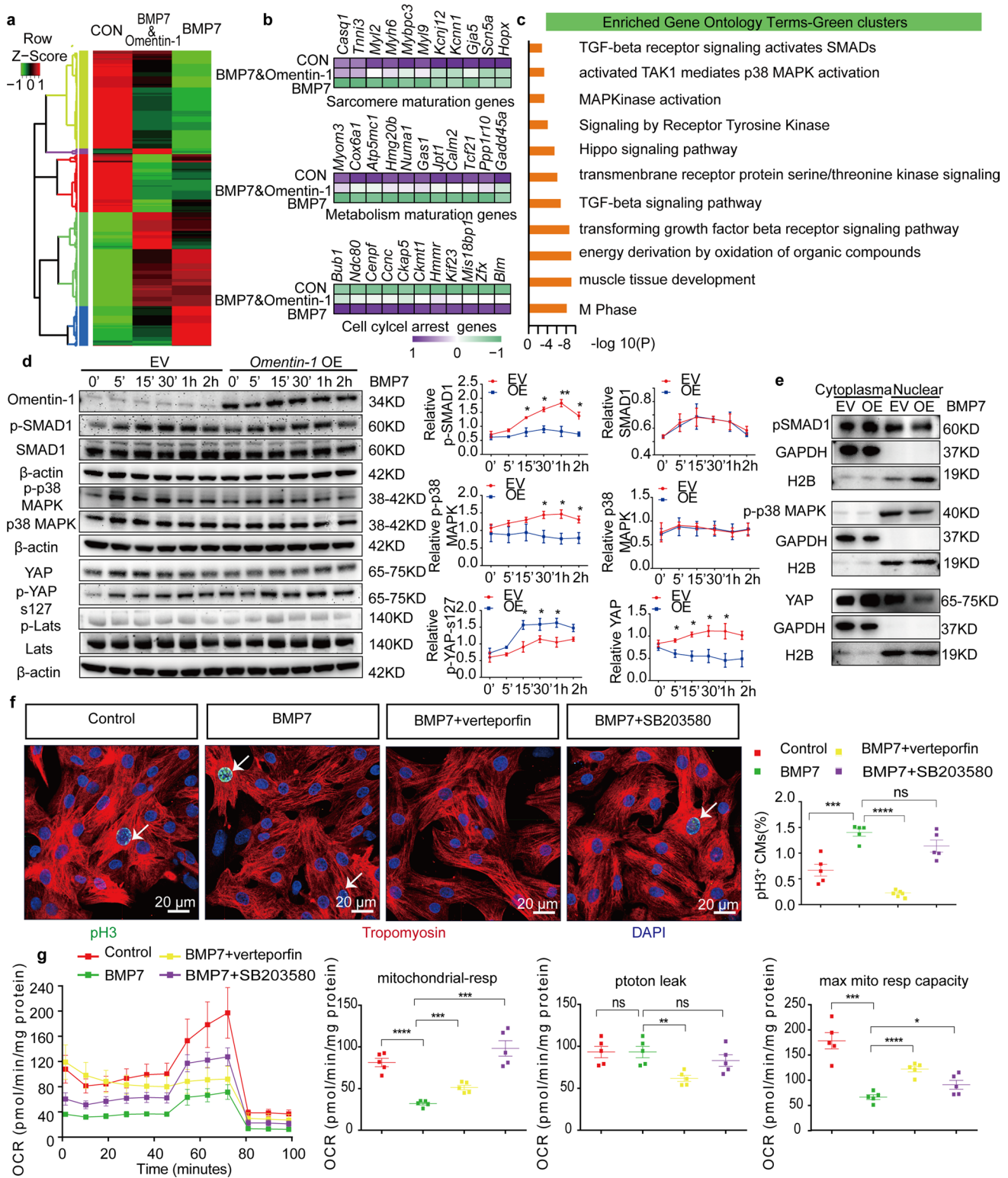
Fig. 6 Omentin-1 antagonized BMP7 signaling via direct interaction. **a** Binding energy calculation for omentin-1 and ActRIIB bound with BMP7. **b** Binding modes (left) of omentin-1 (blue), BMP7 (green), and ActRIIB (red), which are depicted by protein backbone atoms. The hydrogen bonds (right) predicted in omentin-1 and BMP7 (omentin-1: Tyr-297, Glu-274, Lys-198; BMP7: Glu-42, Ala-63, and Glu-60; *Ala* alanine, *Tyr* tyrosine, *Lys* lysine, *Glu* glutamic acid) are shown. **c** Co-immunoprecipitation (Co-IP) assay for the omentin-1 and BMP7 proteins. Primary rat cardiomyocytes (CMs) were lysed and subjected to Co-IP with anti-FLAG antibody beads or anti-BMP7 antibody. Left, Co-IP with omentin-1-flag; right, Co-IP with BMP7. **d** Potential energy plot of three systems (BMP7, BMP7–ActRIIB, and BMP7–omentin-1) over a 30 ns molecular dynamics simulation. The green line represents BMP7, the yellow line represents BMP7–ActRIIB, and blue line represents BMP7–omentin-1. **e** The root-mean-square deviation (RMSD) is the deviation of the protein–ligand complex with respect to the initial minimized structure, which was used to compare the flexibility of the protein backbone during the 30 ns simulation. BMP7 and BMP7–ActRIIB showed similar fluctuations, while the RMSD of BMP7–omentin-1 was lower than those of BMP7 and BMP7–ActRIIB. **f** The root-mean-square fluctuation (RMSF) plots of BMP7, BMP7–ActRIIB, and BMP7–omentin-1 reflect the amino acid fluctuations during simulation. **g** RMSF of BMP7 and omentin-1 showing lower fluctuations in the amino acid residues Lys-126, Ile-124, Asn-122, Asp-119, Trp-55, Arg-48, Tyr-78, Gln-36, Glu-97, and Phe-73. Amino acids in red are the ActRIIB binding site amino acids in BMP7. **h** Representative images of primary rat CMs showing the interaction between BMP7 and ActRIIB. Omentin-1 reduced the interaction. Proximity ligation assay (PLA) signals (in red) indicate BMP7 and ActRIIB interactions; scale bar, 10 μm

omentin-1$^{-/-}$ mice heart (Fig. 2b). *omentin-1*$^{-/-}$ mice hearts were transcriptionally distinct from WT hearts at P14 (299 DEGs) and P30 (1270 DEGs); therefore, these two stages could be considered major developmental divergence stages during postnatal heart development (Fig. 2c). GO analysis showed that the upregulated genes at P14 and P30 were simultaneously enriched in cell cycle pathways, while the downregulated genes were related to cardiac contraction at P14 or OXPHOS at P30 (Supplementary Fig. 3a–d).

To further describe the developmental discrepancy between *omentin-1*$^{-/-}$ and WT mice, we performed WGCNA across these four developmental stages. Eight gene coexpression modules were identified using hierarchical clustering of the similarity and dissimilarity matrix across all transcriptome sets (Fig. 2d, e). Among them, four modules (module

Figure panels a–g showing heatmaps, gene ontology terms, western blots, immunofluorescence images, and OCR measurements.

1: 855 genes, module 2: 1641 genes, module 3: 2765 genes, and module 6: 186 genes) were identified to exhibit significant stage-specific expression correlations in both *omentin-1*$^{-/-}$ and WT mice ($r \geq 0.7$ and $p \leq 0.05$) (Fig. 2f). Module 1 contained genes upregulated gradually during postnatal heart development; these genes were disturbed by *omentin-1* deletion and enriched for the OXPHOS and cardiac muscle contraction GO terms (Fig. 2g, h). Module 2 contained genes involved in fatty acid metabolism and cell cycle arrest, which were specifically upregulated at P30 in WT mice but

◄**Fig. 7** The BMP7/SMAD1/YAP and BMP7/p38 MAPK pathways mediate omentin-1-induced cardiomyocyte (CM) cell cycle arrest and metabolic maturation. **a** Heatmap of gene expression profiles in control CMs, BMP7- and OMT-cotreated CMs, and BMP7-treated CMs. **b** Differential expression analyses of sarcomere, metabolism maturation, and cell cycle arrest genes. The purple-green color scale indicates the differential expression fold change. **c** Gene Ontology (GO) enrichment analysis of differentially expressed genes in green clusters. **d** Western blot analysis showing time-dependent changes in BMP7 signaling downstream proteins, including SMAD1, p-SMAD1, YAP, p-YAP, p38 MAPK, and p-p38MAPK (left). Primary CMs were pretreated with an empty virus control (EV) and *omentin-1* overexpression (OE) virus and then stimulated with BMP7 protein (100 ng/ml). The phosphorylation levels were determined by corresponding band intensity measurements, and the values were determined relative to β-actin signals. **e** Western blot analysis detected p-SMAD1, p-YAP, and p-p38 MAPK proteins in the cytoplasm and nuclear fraction in EV/*omentin-1*-OE CMs with BMP7 stimulation. **f** Immunofluorescence of primary rat CM proliferation (pH3) in response to BMP7, BMP7+YAP inhibitor (verteporfin), and BMP7+MAPK inhibitor (SB203580); scale bar, 20 μm. **g** Mitochondrial stress assay demonstrating the mitochondrial respiration and proton leak in four primary rat CM groups; the PBS control, BMP7, BMP7+MAPK inhibitor (SB203580), and BMP7+YAP inhibitor (verteporfin) groups. ****$p < 0.0001$, ***$p < 0.001$, **$p < 0.01$, *$p < 0.05$ by unpaired Student's t test

significantly downregulated in *omentin-1*$^{-/-}$ mice (Fig. 2i, j). Module 3 included a large number of cell cycle genes whose expression continually decreased during postnatal development and were upregulated in *omentin-1*$^{-/-}$ mice at P14 (Fig. 2k, l). Module 6 was composed mainly of ion transport genes, which were disordered at P14 and P30 in *omentin-1*$^{-/-}$ mice (Fig. 2m, n). Density plot analysis also revealed that omentin-1 deficiency suspended postnatal heart development processes, including cell cycle arrest, fatty acid metabolism, and contraction at P14 and P30 (Fig. 2o and Supplementary Fig. 3e). Collectively, these results indicate that omentin-1 deficiency leads to CM maturation retardation in juveniles by delaying cell cycle arrest at P14 and metabolic switching at P30.

## Omentin-1 deficiency suspends CM cell cycle arrest and metabolic maturation

To investigate whether omentin-1 drives CM maturation during postnatal heart development, we measured CM proliferation at P14 in *omentin-1*$^{-/-}$ mice. We found that *omentin-1* deletion had no effect on HW/TL at P14 (Fig. 3a). Wheat germ agglutinin (WGA) staining revealed that the CM area of *omentin-1*$^{-/-}$ mice was significantly smaller than that of WT mice (Fig. 3b). We also isolated CMs from P14 mouse hearts and found that the widths of CMs decreased (Fig. 3c) as the CM count increased (Fig. 3d) once omentin-1 was absent, indicating that *omentin-1* deletion enhances CM proliferation. Then, we detected CM proliferation in P14 hearts by staining for the mitosis marker pH3 and the

cytokinesis marker Aurora B kinase. Immunofluorescence staining showed that the proportion of pH3$^+$α-actinin$^+$ CMs was increased in *omentin-1*$^{-/-}$ mice (Fig. 3e and Supplementary Fig. 4a). Aurora B kinase, which is expressed in the cleavage furrow between two proliferating CMs, was upregulated in *omentin-1*$^{-/-}$ mice hearts (Fig. 3f and Supplementary Fig. 4b). Moreover, cyclin D1 and cyclin-dependent kinase (CDK2) expression was upregulated in the *omentin-1*$^{-/-}$ mice heart (Supplementary Fig. 5a), indicating that omentin-1 deficiency enhances the proliferative capacity of CMs, delaying CM cell cycle arrest at P14.

Another effective indicator of CM maturation is metabolism. To assess the metabolic maturation of *omentin-1*$^{-/-}$ mice hearts, we prepared myocardial tissue from P30 mouse hearts and detected metabolism with high-resolution respirometry OROBOROS. In line with the findings of previous studies [51, 52], the OCRs were determined by subsequently adding fatty acid substrates (malate, octanoyl-carnitine, and ADP) and citrate cycle-derived substrates (glutamate and succinate). With fatty acid substrates present, the β-oxidation-linked respiration of the *omentin-1*$^{-/-}$ mice hearts was 44% lower than that of WT hearts (Fig. 3g). Following the introduction of citrate cycle-derived substrates, the mitochondrial OXPHOS respiratory ability of *omentin-1*$^{-/-}$ mice hearts was 37% lower than that of WT hearts (Fig. 3g). The mitochondrial respiratory control ratio was significantly reduced and the leak control ratio increased in *omentin-1*$^{-/-}$ mice hearts (Fig. 3h), suggesting a deterioration in mitochondrial coupling efficiency upon omentin-1 deficiency. Transmission electron microscopy (TEM) measurements revealed smaller and less dense mitochondria in *omentin-1*$^{-/-}$ mice hearts (Supplementary Fig. 5b) than in WT hearts. Additionally, mitochondrial DNA content was lower in the hearts of *omentin-1*$^{-/-}$ mice (Supplementary Fig. 5c), as were the levels of OXPHOS proteins (Supplementary Fig. 5d). These results suggest that omentin-1 deficiency reduces metabolic maturation.
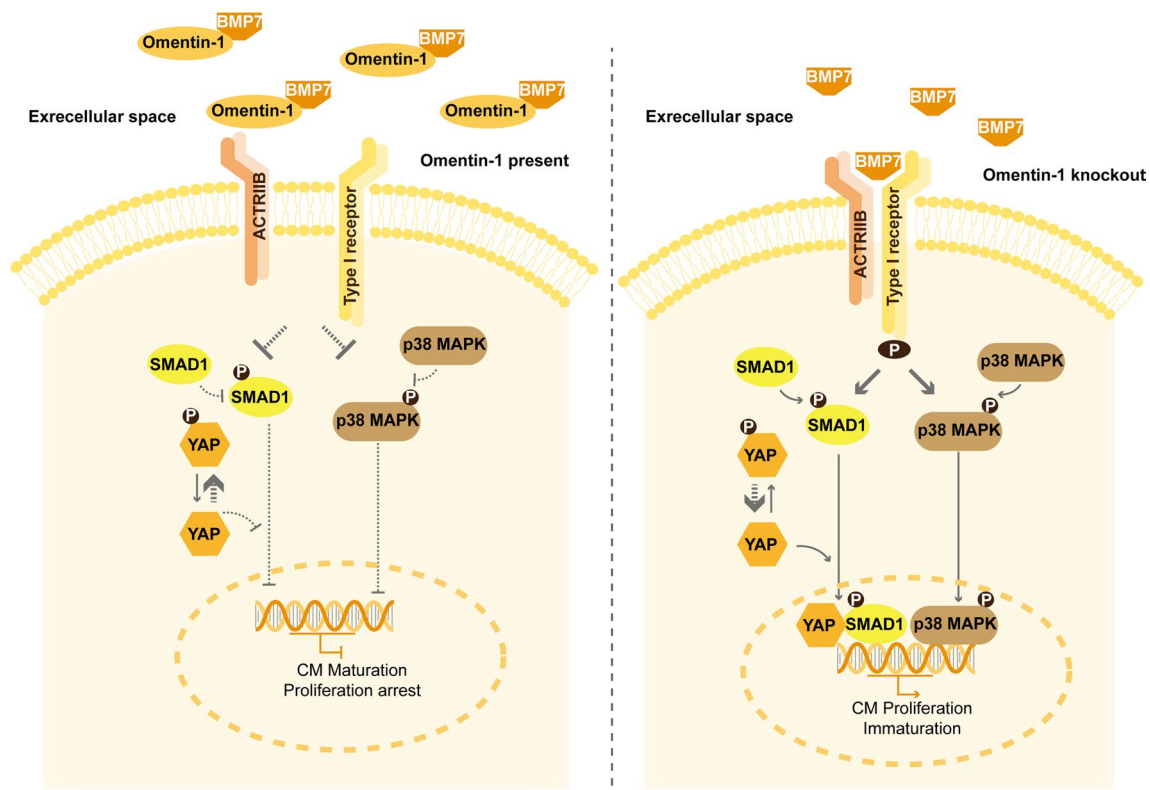
Omentin-1 facilitates CM cell cycle arrest and metabolic maturation

To explore whether omentin-1 is sufficient for CM maturation, we treated primary CMs isolated from neonatal rats with omentin-1. CMs were treated with a physiologic concentration of recombinant human omentin-1 protein (300 ng/ml) for 48 h (Fig. 4a). We found that omentin-1 led CMs to become enlarged and rod-shaped and caused sarcomere densification (according to immunofluorescence staining with α-actinin) under microscopic observation (Fig. 4b). Immunostaining revealed that the proportions of mitotic CMs (pH3$^+$α-actinin$^+$) and cytokinetic CMs (Aurora B$^+$α-actinin$^+$) decreased after omentin-1 treatment (Fig. 4c, d). Flow cytometry showed that EdU
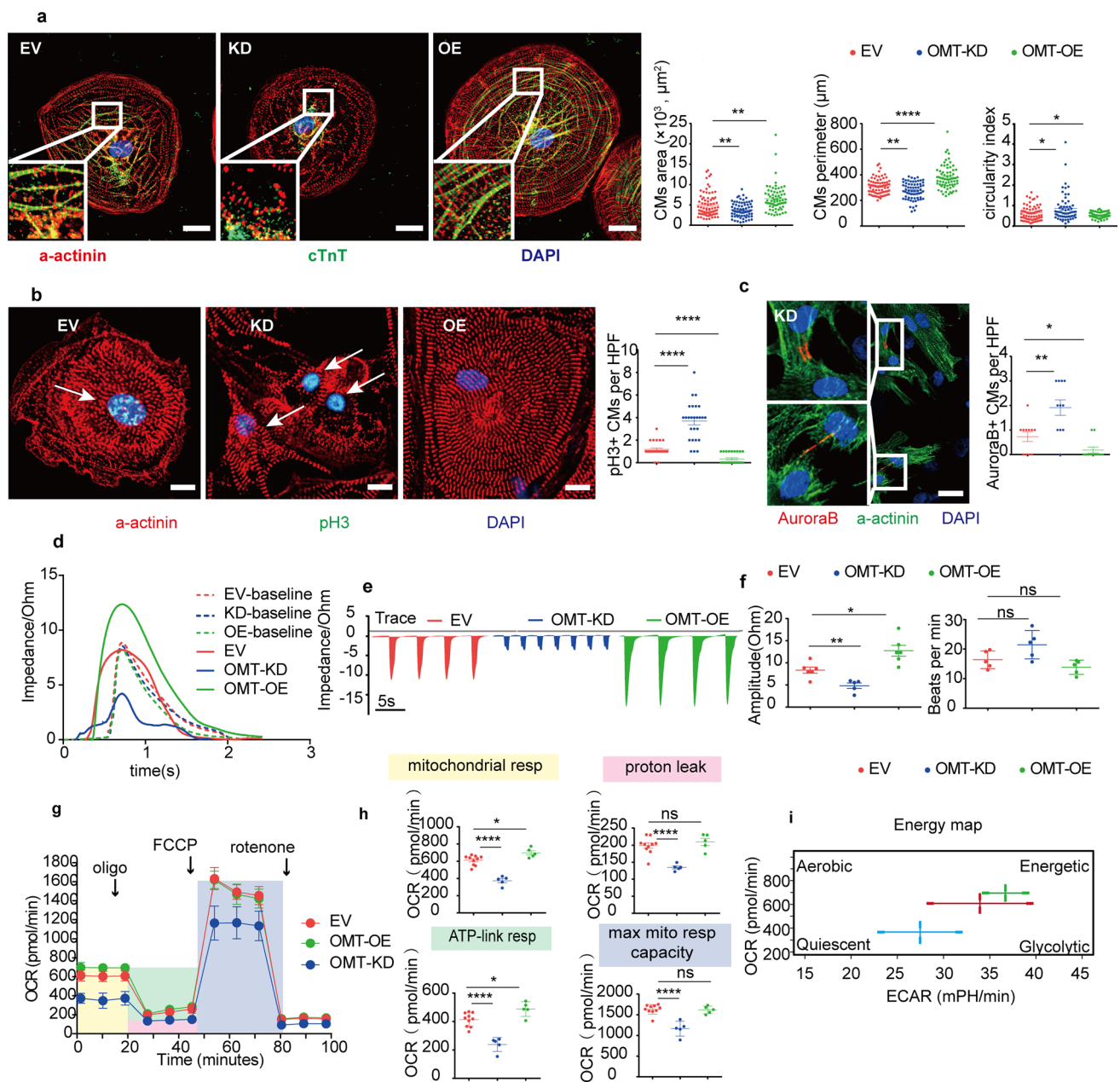
Fig. 8 Omentin-1 is required and sufficient for human embryonic stem cell-derived cardiomyocyte (hES-CM) cell cycle arrest and metabolic maturation. **a** Compared with the empty vector (EV) control CMs, *omentin-1* knockdown (KD) or overexpression (OE) CMs showed significant changes in cell perimeter, cell area, and circularity index. Approximately 70 cells per group, three biological replicates. OMT-KD, *omentin-1* knockdown; OMT-OE, *omentin-1* overexpression; EV, empty vector. **b** Assessment of mitotic activity by pH3 immunostaining. Representative images and quantification of pH3$^+$ CMs per high-power filed (HPF). **c** Assessment of cytokinesis activity by Aurora B immunostaining. Representative images and quantification of Aurora B$^+$ CMs per high HPF. **d**–**f** CardioExcyte 96 function analysis. Representative CM beating amplitude **d** in CMs at baseline (day 16) and after transduction at day 30. In addition, represent beating traces **e** in EV control, *omentin-1*-KD, and *omentin-1*-OE CMs at day 30. A significant change in beating amplitude and rela-tive changes in beating rates **f** in *omentin-1*-KD and *omentin-1*-OE CMs are shown. Fifty thousand CMs per sample and 5–6 samples per group. **g** Representative OCR profile in response to the ATP synthase inhibitor oligomycin, the electron transport and OXPHOS uncoupler FCCP, and the electron transport chain blocker rotenone during the Mito Stress Test assay. **h** Quantification of mitochondrial respiration, proton leak, ATP-linked respiration, and maximum mitochondrial respiration capacity in EV, *omentin-1*-KD, and *omentin-1*-OE CMs. There were 10 samples in the EV groups and 5 samples in the OMT-KD or OMT-OE groups. **i** Energy map of EV control, *omentin-1*-KD, and *omentin-1*-OE CMs. The oxygen consumption rate (OCR) and extracellular acidification rate (ECAR) shown in the map were the basal OCR and ECAR simultaneously derived from the Mito Stress Test. The other procedures for the OE group and the KD group were the same. The data are presented as the mean $\pm$ SEM. ****$p < 0.0001$, **$p < 0.01$, *$p < 0.05$ by unpaired Student's *t* test

Fig. 9 Model of BMP7–omentin-1 in cardiomyocyte (CM) cell cycle arrest and metabolic maturation. The expression of omentin-1 is upregulated during postnatal heart development. Omentin-1 binds to BMP7 extracellularly, prevents BMP7 from binding to its receptor ActRIIB, and blocks the SMAD1/YAP and p38 MAPK pathways, which induces CM maturation and cell cycle arrest. BMP7, bone morphogenetic protein 7; SMAD1, mothers against DPP homolog 1; p38 MAPK, p38 mitogen-activated protein kinase; YAP, yes-associated protein; ActRIIB, activin type II receptor B

incorporation was decreased in omentin-1-treated CMs, which was also confirmed by immunostaining (Supplementary Fig. 6a, b), suggesting that DNA synthesis of CM was reduced upon omentin-1 treatment. Moreover, we found that omentin-1 increased the percentage of quiescent CMs (G0/G1) (Fig. 4e) without apoptosis (Supplementary Fig. 6c), indicating that omentin-1 facilitates cell cycle arrest.

Following treatment with omentin-1, the content and distribution of the mitochondrial marker Tom20 increased significantly (Fig. 4f). JC-1 flow cytometry analysis demonstrated that mitochondrial activity, as reflected by JC-1 aggregate formation, was significantly elevated upon omentin-1 treatment (Fig. 4g). In addition, the maximal respiration rates were increased in omentin-1-treated CMs, as quantified by OCR analysis (Fig. 4h). CM glycolysis, as measured by ECAR assessment, decreased under omentin-1 treatment (Fig. 4i). An increase in mitochondrial respiration with reduced glycolysis suggests a role for omentin-1 in enhancing metabolic maturation in CMs.

Then, we administered omentin-1 continuously to mice (1 µg/g per mouse) from P1 to P7 via multiple back subcutaneous injections and measured CM maturation at P7. Immunostaining showed that omentin-1 promoted CM maturation processes, including cell area enlargement (WGA$^+$) (Supplementary Fig. 6d), cell cycle arrest (pH3$^+$) (Supplementary Fig. 6e), and mitochondrial distribution increases (Tom20$^+$) (Supplementary Fig. 6f), suggesting that omentin-1 accelerates CM maturation in vivo. Together, these findings demonstrate that omentin-1 inhibits CM proliferation and promotes metabolic maturation.

Omentin-1 regulates CM maturation via blocking BMP7 signaling

To investigate the mechanism by which omentin-1 regulates CM maturation, we performed upstream regulator analysis of DEGs in the transcriptome profile between *omentin-1$^{-/-}$* and WT mice. We focused on the P14 and P30 stages because omentin-1 deficiency mainly disturbed the cardiac gene expression profile at these two stages (Fig. 2c). IPA was used to identify upstream regulators of *omentin-1$^{-/-}$* hearts,

and 20 upstream regulators at P14 and 140 upstream regulators at P30 were identifed as significantly changed (Supplementary Table 3, 4). Eight target regulators, *Bmp7*, *Hells*, *Brac1*, *Ccna2*, *Plk1*, *Mybl2*, *Snca* and *Lart*, overlapped in these two stages (Fig. 5a). These regulators were also enriched in metabolic and other cellular processes based on Metascape analysis (Fig. 5b). qRT-PCR showed that *Bmp7*, *Hells*, *Brac1*, *Ccna2*, *Plk1*, and *Mybl2* were significantly upregulated in *omentin-1$^{-/-}$* hearts, while *Snca* and *Lart* were not different between WT and *omentin-1$^{-/-}$* hearts at P14 (Fig. 5c). Among these six regulators, HELLS, BARC1, CCNA2, PLK1, and MYBL2 are localized intracellularly, while BMP7 can be secreted outside of cells [53]. It has been reported that omentin-1 can interact with extracellular proteins to perform its function [54], and regulators localized in the cell (*Hells*, *Barc1*, *Ccna2*, *Plk1*, and *Mybl2*) may not be directly affected by omentin-1. Therefore, we hypothesized that omentin-1 might regulate CM maturation through extracellular interaction with the extracellular protein BMP7.

To uncover the role of BMP7 in CM proliferation and metabolism maturation, we treated primary neonatal rat CMs with recombinant BMP7 (100 ng/ml) for 48 h. After BMP7 treatment, CMs behaved as immature, with a small size (α-actinin$^+$) (Fig. 5d), a pro-proliferative phenotype (pH3$^+$ CMs) (Fig. 5e), a reduced mitochondrial distribution (Tom20$^+$ CMs) (Fig. 5f), a decrease in mitochondrial respiratory capacity, and an increase in glycolytic capacity (Fig. 5g, h), which suggests that BMP7 promotes CM proliferation while reducing the energy directed to maturation. Furthermore, the effect of BMP7 on CMs was inhibited by cotreatment with recombinant omentin-1 (300 ng/ml) (Fig. 5d–h). Together, these results suggest that omentin-1 controls CM maturation through its antagonistic effects on BMP7.

Omentin-1 antagonizes BMP7 signaling by competitively blocking BMP7 binding to ActRIIB

To investigate how omentin-1 antagonizes BMP7, we performed protein−protein docking and predicted that the shape energy of the binding of omentin-1 to BMP7 was similar to that of the binding of BMP7 to its receptor, ActRIIB (Fig. 6a). Superposition of omentin-1 onto the BMP7−ActRIIB complex revealed that the binding site for BMP7 overlapped in omentin-1 and ActRIIB (Fig. 6b and Supplementary Fig. 7a), suggesting that omentin-1 may interact with BMP7. We constructed a plasmid expressing flag-omentin-1 fusion protein and overexpressed it in CMs. Co-IP using flag and BMP7 antibodies showed that these two proteins were able to interact with each other (Fig. 6c).

Then, we assessed the impact on BMP7 after interaction with omentin-1 by molecular dynamics simulation. After 30 ns of simulation, the models of BMP7, BMP7−ActRIIB,

and BMP7−omentin-1 were equilibrated (Fig. 6d). The root-mean-square deviation (RMSD) plot of the three models demonstrated that the RMSD change of BMP7−ActRIIB was similar to that of BMP7 but significantly higher than that of BMP7−omentin-1, suggesting that the structure of BMP7 was stable within the ActRIIB interaction but sharply changed within the omentin-1 interaction (Fig. 6e). We next calculated the root-mean-square fluctuation (RMSF) and found that the RMSF of the ActRIIB binding site amino acids of BMP7, including Lys-126, Ile-124, Asn-122, Asp-119, and Trp-55, significantly fluctuated when omentin-1 interacted with BMP7 (Fig. 6f, g). This finding suggests that omentin-1 may partly cover the BMP7−ActRIIB binding site. Using a Duolink PLA, we confirmed that omentin-1 interferes with BMP7 binding to the receptor ActRIIB in CMs (Fig. 6h). Together, these results suggest that omentin-1 interacts with BMP7 and prevents BMP7 from binding to its receptor ActRIIB, which blocks BMP7 signaling.

Omentin-1 suppresses the downstream pathways of BMP7

To uncover the downstream pathways of BMP7 affected by omentin-1 in CMs, we profiled transcriptome changes in BMP7 and BMP7-/omentin-1-cotreated CMs. RNA-seq revealed that 1381 genes responded to BMP7 stimulation. More than half of these genes (1090 genes) were antagonized by omentin-1, as shown by unsupervised hierarchical clustering analysis (see the yellow, green, and blue cluster in Fig. 7a). The expression of several key regulators of CM maturation was attenuated by BMP7 treatment but blocked by omentin-1 and BMP7 cotreatment (Fig. 7b). GO analysis of BMP7-activated genes (green and blue clusters) revealed that SMADs, p38 MAPK, and Hippo signaling were upregulated in response to BMP7 stimulation but downregulated upon cotreatment with omentin-1 (Fig. 7c and Supplementary Fig. 7b). Then, analysis of BMP7-treated, omentin-1-treated, and BMP7- and omentin-1-cotreated CMs confirmed that BMP7 induced SMAD1, p38 MAPK, and YAP activation, while BMP7 and omentin-1 cotreatment inhibited these pathways (Supplementary Fig. 7c).

SMAD1 and p38 MAPK are canonical and noncanonical signaling molecules of BMP7, respectively. To further examine the blocking effect of omentin-1 on BMP7, a time-dependent study was performed on CMs overexpressing omentin-1 and activated by BMP7. Following BMP7 stimulation, SMAD1 or p38 MAPK phosphorylation was increased in EV-transduced CMs and peaked after 60 min, whereas activation was significantly decreased in *omentin-1*-OE CMs (Fig. 7d). In addition, Western blot analysis demonstrated that BMP7-mediated YAP expression was increased in EV CMs, whereas YAP expression was decreased and phosphorylated YAP levels were increased (phospho-YAP-serine 127, p-YAP-S127) in

omentin-1-OE CMs, even though LATS kinase activity was not altered (Fig. 7d). As SMAD1 has previously been reported to contribute to cell proliferation by forming a complex with YAP that promotes the nuclear localization of YAP [55], we performed nucleoplasm separations to investigate the influence of SMAD1 on the YAP pathway. *Omentin-1*-OE CMs stimulated with BMP7 displayed reduced nuclear localization of SMAD1, p38 MAPK, and YAP and enhanced cytoplasmic retention of SMAD1 and YAP (Fig. 7e). In Co-IP analysis, YAP binding to SMAD1 was decreased in *omentin-1*-OE CMs when stimulated with BMP7, indicating that omentin-1 inhibits the activation of SMAD1 by BMP7, thereby decreasing SMAD1-YAP complex formation and decreasing YAP nuclear translocation (Supplementary Fig. 7d). Together, these results demonstrate that omentin-1 inhibits BMP7-driven SMAD1, p38 MAPK, and YAP pathway activation.

To evaluate the function of SMAD1/YAP or p38 MAPK in CM maturation, we treated primary CMs with their inhibitors (Supplementary Fig. 7e, f). We found that YAP inhibition (with verteporfin) but not p38 MAPK inhibition (with SB203580) significantly reduced BMP7-induced CM proliferation (Fig. 7f). In a mitochondrial stress assay (Fig. 7g), and a glycolysis stress assay (Supplementary Fig. 7 g), BMP7-induced CM metabolic immaturity was improved by both p38 MAPK inhibition and YAP inhibition. Collectively, our results suggest that omentin-1 reduces BMP7 activity, accelerating CM cell cycle arrest via SMAD1/YAP pathways and promoting CM metabolic maturation via both SMAD1/YAP and p38 MAPK pathways.

Omentin-1 is required and sufficient for the maturation of hES-CMs

To assess the translational potential of omentin-1, we evaluated whether omentin-1 affects the maturation of hES-CMs (Supplementary Fig. 8a). We used flow cytometry to determine cell purity. The purity of hES-CMs was above 85% after purification on day 16 and then cultured to day 30 (Supplementary Fig. 8b). *Omentin-1* gene expression was knocked down effectively with shRNA introduced by lentivirus at day 16, and the maturation phenotypes were examined on day 30 (Supplementary Fig. 8c–d). We found that *omentin-1* knockdown caused sarcomere disarrangement with decreases in cell area and perimeter (Fig. 8a). Immunostaining revealed that *omentin-1* knockdown induced hES-CM proliferation (Fig. 8b, c). The CE96 function analysis system demonstrated that *omentin-1*-KD hES-CMs had a reduced beating amplitude and a relatively increased beating rate (Fig. 8d–f). The real-time OCR measurements demonstrated that the baseline mitochondrial respiration, ATP-linked respiration, proton leak, and maximum respiration capacity were reduced in *omentin-1*-KD hES-CMs

(Fig. 8g–i). Taken together, coinciding with our findings in mice, these results indicate that omentin-1 deficiency disturbs hES-CM morphology, proliferation, contraction, and metabolic maturation.

To examine whether omentin-1 is sufficient to promote hES-CM maturation, omentin-1 was overexpressed by lentivirus on day 16 (Supplementary Fig. 8c-d). The procedures used for the OE group were the same as those used for the KD group. Immunostaining revealed that *omentin-1* overexpression led sarcomeres to acquire a more regular and dense arrangement (Fig. 8a) and to undergo cell cycle arrest (Fig. 8b, c) on day 30. We also found that *omentin-1*-OE hES-CMs exhibited a significantly higher beating amplitude and lower beating rate than cells infected with the EV control (Fig. 8d–f). *Omentin-1* overexpression also upregulated basal mitochondrial respiration and ATP-linked respiration in hES-CMs with a decrease in proliferation (Fig. 8g–i). Collectively, our results indicated that omentin-1 is required and sufficient for hES-CM cell cycle arrest and metabolic maturation.

Discussion

In this study, we found that omentin-1 plays an essential role in CM maturation during postnatal heart development and propose a working model (depicted in Fig. 9). Omentin-1 interacts with BMP7 extracellularly, preventing BMP7 from binding to ActRIIB, which inactivates SMAD1/YAP and p38 MAPK nuclear translocation to promote CM cell cycle arrest and metabolic maturation.

Our results showed that omentin-1 deficiency leads to heart progressively enlargement and dysfunction in mice, which corresponds to the low level of serum omentin-1 in patients with heart failure [35, 56]. Omentin-1 deletion-mediated heart failure is similar to the effects of other adipokines, such as apelin [30] and adiponectin [31, 57], indicating the essential roles of adipokines in maintaining heart function. Consistent with the notion that long-term dedifferentiation or dematuration deteriorates cardiac function [58], *omentin-1*$^{-/-}$ mice exhibited cardiac maturation retardation and progressively developed heart failure. Transcriptome sequencing of *omentin-1*$^{-/-}$ mice showed that the expression of CM maturation-related genes fluctuated during postnatal heart development, similar to the findings of previous studies [59, 60].

Omentin-1 is a multifunctional adipocytokine [36, 40, 61–65]. Previous studies have found that omentin-1 has anti-inflammatory, antiatherosclerotic and cardiovascular-protective effects [66], and that its circulating levels are negatively correlated with obesity [67–70], type 2 diabetes [69], insulin resistance [71], atherosclerosis [72], bone metabolic diseases [73], inflammatory bowel disease [74], polycystic ovary

syndrome [64, 71], and sleep apnea syndrome [65]. Omentin-1 prevents myocardial hypertrophy induced by transverse aortic constriction [37] and glucocorticoid-induced cardiac injuries [75]. In addition, high plasma omentin-1 levels are associated with improved coronary collateral circulation development [76]. Our results demonstrated that omentin-1 drove CM cell cycle arrest and metabolic maturation.

In terms of cell proliferation, omentin-1 has been found to suppress the growth of colon cancer stem cells [77], neuroblastoma cells [78] and gastric cancer cells [79], and to significantly inhibit the proliferation of HepG2 and HuH-7 human hepatocellular carcinoma cells [80]. Similarly, omentin-1 significantly suppresses PDGF-BB-induced human aortic smooth muscle cell proliferation [72], and FBS-induced smooth muscle cell outgrowth from isolated rat mesenteric arteries [81]. Consistent with these findings, our results showed that omentin-1 effectively inhibited the proliferation of CMs, an effect that was conserved in hES-CMs and mouse primary CMs. In contrast, omentin-1 was confirmed to stimulate the proliferation of neural stem cells [82], mesenchymal stem cells [83], human nucleus pulposus cells [84] and human osteoblasts [85]. These differences may have been due to the different cell types used in these studies.

Regarding the effects of omentin-1 on cellular metabolism, Yang et al. [86] found that omentin-1 enhanced insulin-stimulated glucose uptake in adipocytes. Several clinical studies have reported that serum omentin-1 levels are significantly decreased in patients with type 2 diabetes, obesity, insulin resistance and metabolic syndrome [69, 87–90]. In addition, omentin-1 has been demonstrated to promote mitochondrial biogenesis in chondrocytes [91]. Omentin-1 also improves cardiac mitochondrial function by, for example, reducing lipid deposition, inducing mitochondrial biogenesis, and enhancing mitochondrial activities [75]. In our study, omentin-1 promoted mitochondrial OXPHOS of CMs instead of glycolysis. This may have been due to the unique energy metabolism characteristics of CMs: in these cells, ATP is produced by the oxidation of mainly fatty acids rather than glucose.

We found that omentin-1 blocked BMP7 activity by preventing BMP7-receptor binding outside of the cell. Previous studies have also reported that BMP7 activity can be regulated extracellularly by secreted proteins such as noggin [92], myostatin [93], and coagulation factor XI [94]. BMP7 plays vital roles in nephrogenesis, osteogenesis, neurogenesis, and adipocyte differentiation during development [95–97] and represses CM hypertrophy [53], cardiac fibrosis [98], and inflammation in the myocardium [99]. In this study, we found that BMP7 promoted CM proliferation and attenuates CM metabolic maturation, which could be suspended by omentin-1. We also found that SMAD1-YAP and p38 MAPK signaling could be activated by BMP7 simultaneously. SMAD1-YAP nuclear translocation [100] stimulated by BMP7 regulates CM proliferation and promotes glycolysis. On the other hand, p38 MAPK only participated in BMP7-mediated mitochondrial respiration suppression.

In summary, we have identified a crucial role of omentin-1 in CM proliferation and metabolism maturation during postnatal heart development. The absence of omentin-1 causes a severe cardiac phenotype that includes ventricular enlargement and cardiac dysfunction. Omentin-1 regulates CM maturation by binding to BMP7, which is an activator of SMAD1-YAP and p38 MAPK signaling in CMs. The pro-maturation function of omentin-1 is conserved in hES-CMs, indicating that omentin-1 is a promising target for cardiac diseases.

Data availability The sequencing datasets involved in this work have been deposited in the NCBI database under project accession number PRJNA681365.

Declarations

Conflict of interest The authors declare no competing interests.

Ethical approval The animal experiments were conducted in accordance with the Guide for the Use and Care of Laboratory Animals. All animal protocols were approved by the Institutional Animal Care

and Use Committee (IACUC), Fuwai Hospital, Chinese Academy of Medical Sciences.

Consent for publication All the authors have consented to publication in CMLS.

References

1. Zaffran S, Frasch M (2002) Early signals in cardiac development. Circ Res 91:457–469. https://doi.org/10.1161/01.res.00000 34152.74523.a8
2. Guo Y, Pu WT (2020) Cardiomyocyte maturation: new phase in development. Circ Res 126:1086–1106. https://doi.org/10.1161/CIRCRESAHA.119.315862
3. Kannan S, Kwon C (2020) Regulation of cardiomyocyte maturation during critical perinatal window. J Physiol 598:2941–2956. https://doi.org/10.1113/JP276754
4. Sim CB, Phipson B, Ziemann M et al (2021) Sex-specific control of human heart maturation by the progesterone receptor. Circulation 143:1614–1628. https://doi.org/10.1161/CIRCULATIONAHA.120.051921
5. Puente BN, Kimura W, Muralidhar SA et al (2014) The oxygen-rich postnatal environment induces cardiomyocyte cell-cycle arrest through DNA damage response. Cell 157:565–579. https://doi.org/10.1016/j.cell.2014.03.032
6. Li Y, Feng J, Song S et al (2020) gp130 controls cardiomyocyte proliferation and heart regeneration. Circulation 142:967–982. https://doi.org/10.1161/CIRCULATIONAHA.119.044484
7. Li R, Xiang C, Li Y, Nie Y (2023) Targeting immunoregulation for cardiac regeneration. J Mol Cell Cardiol 177:1–8. https://doi.org/10.1016/j.yjmcc.2023.02.003
8. Wang Y, Li Y, Feng J et al (2020) Mydgf promotes cardiomyocyte proliferation and neonatal heart regeneration. Theranostics 10:9100–9112. https://doi.org/10.7150/thno.44281
9. Guo Y, Cao Y, Jardin BD et al (2021) Sarcomeres regulate murine cardiomyocyte maturation through MRTF-SRF signaling. Proc Natl Acad Sci U S A. https://doi.org/10.1073/pnas.2008861118
10. Fukuda R, Gunawan F, Ramadass R et al (2019) Mechanical forces regulate cardiomyocyte myofilament maturation via the VCL-SSH1-CFL axis. Dev Cell 51:62–77. https://doi.org/10.1016/j.devcel.2019.08.006
11. Gong G, Song M, Csordas G, Kelly DP, Matkovich SJ, Dorn GW 2nd (2015) Parkin-mediated mitophagy directs perinatal cardiac metabolic maturation in mice. Science 350:aad2459. https://doi.org/10.1126/science.aad2459
12. Kuppusamy KT, Jones DC, Sperber H et al (2015) Let-7 family of microRNA is required for maturation and adult-like metabolism in stem cell-derived cardiomyocytes. Proc Natl Acad Sci U S A 112:E2785-2794. https://doi.org/10.1073/pnas.1424042112
13. Lopaschuk GD, Jaswal JS (2010) Energy metabolic phenotype of the cardiomyocyte during development, differentiation, and postnatal maturation. J Cardiovasc Pharmacol 56:130–140. https://doi.org/10.1097/FJC.0b013e3181e74a14
14. Wilsbacher L, McNally EM (2016) Genetics of cardiac developmental disorders: cardiomyocyte proliferation and growth and relevance to heart failure. Annu Rev Pathol 11:395–419. https://doi.org/10.1146/annurev-pathol-012615-044336
15. Ai S, Peng Y, Li C et al (2017) EED orchestration of heart maturation through interaction with HDACs is H3K27me3-independent. Elife. https://doi.org/10.7554/eLife.24570
16. Liang X, Sun Y, Ye M et al (2009) Targeted ablation of PINCH1 and PINCH2 from murine myocardium results in dilated cardiomyopathy and early postnatal lethality. Circulation 120:568–576. https://doi.org/10.1161/CIRCULATIONAHA.109.864686
17. Hu P, Liu J, Zhao J, Wilkins BJ, Lupino K, Wu H, Pei L (2018) Single-nucleus transcriptomic survey of cell diversity and functional maturation in postnatal mammalian hearts. Genes Dev 32:1344–1357. https://doi.org/10.1101/gad.316802.118
18. Liu C, Spinozzi S, Chen JY et al (2019) Nexilin Is a new component of junctional membrane complexes required for cardiac T-tubule formation. Circulation 140:55–66. https://doi.org/10.1161/CIRCULATIONAHA.119.039751
19. Metrich M, Bezdek Pomey A, Berthonneche C, Sarre A, Nemir M, Pedrazzini T (2015) Jagged1 intracellular domain-mediated inhibition of Notch1 signalling regulates cardiac homeostasis in the postnatal heart. Cardiovasc Res 108:74–86. https://doi.org/10.1093/cvr/cvv209
20. Parikh SS, Blackwell DJ, Gomez-Hurtado N et al (2017) Thyroid and glucocorticoid hormones promote functional T-tubule development in human-induced pluripotent stem cell-derived cardiomyocytes. Circ Res 121:1323–1330. https://doi.org/10.1161/CIRCRESAHA.117.311920
21. Sakamoto T, Matsuura TR, Wan S et al (2020) A critical role for estrogen-related receptor signaling in cardiac maturation. Circ Res 126:1685–1702. https://doi.org/10.1161/CIRCRESAHA.119.316100
22. Guo Y, Jardin BD, Zhou P et al (2018) Hierarchical and stage-specific regulation of murine cardiomyocyte maturation by serum response factor. Nat Commun 9:3837. https://doi.org/10.1038/s41467-018-06347-2
23. Mahmoud AI, Kocabas F, Muralidhar SA et al (2013) Meis1 regulates postnatal cardiomyocyte cell cycle arrest. Nature 497:249–253. https://doi.org/10.1038/nature12054
24. Nguyen NUN, Canseco DC, Xiao F et al (2020) A calcineurin-Hoxb13 axis regulates growth mode of mammalian cardiomyocytes. Nature 582:271–276. https://doi.org/10.1038/s41586-020-2228-6
25. Chattergoon NN, Giraud GD, Louey S, Stork P, Fowden AL, Thornburg KL (2012) Thyroid hormone drives fetal cardiomyocyte maturation. FASEB J 26:397–408. https://doi.org/10.1096/fj.10-179895
26. Chattergoon NN, Louey S, Scanlan T, Lindgren I, Giraud GD, Thornburg KL (2019) Thyroid hormone receptor function in maturing ovine cardiomyocytes. J Physiol 597:2163–2176. https://doi.org/10.1113/JP276874
27. Bassat E, Mutlak YE, Genzelinakh A et al (2017) The extracellular matrix protein agrin promotes heart regeneration in mice. Nature 547:179–184. https://doi.org/10.1038/nature22978
28. Lau WB, Ohashi K, Wang Y, Ogawa H, Murohara T, Ma XL, Ouchi N (2017) Role of adipokines in cardiovascular disease. Circ J 81:920–928. https://doi.org/10.1253/circj.CJ-17-0458
29. Smekal A, Vaclavik J (2017) Adipokines and cardiovascular disease: A comprehensive review. Biomed Pap Med Fac Univ Palacky Olomouc Czech Repub 161:31–40. https://doi.org/10.5507/bp.2017.002
30. Kuba K, Zhang L, Imai Y et al (2007) Impaired heart contractility in Apelin gene-deficient mice associated with aging and pressure overload. Circ Res 101:e32-42. https://doi.org/10.1161/CIRCRESAHA.107.158659
31. Liao Y, Takashima S, Maeda N et al (2005) Exacerbation of heart failure in adiponectin-deficient mice due to impaired regulation of AMPK and glucose metabolism. Cardiovasc Res 67:705–713. https://doi.org/10.1016/j.cardiores.2005.04.018
32. Hall ME, Smith G, Hall JE, Stec DE (2012) Cardiomyocyte-specific deletion of leptin receptors causes lethal heart failure in Cre-recombinase-mediated cardiotoxicity. Am J Physiol

Regul Integr Comp Physiol 303:R1241-1250. https://doi.org/10.1152/ajpregu.00292.2012

33. McGaffin KR, Witham WG, Yester KA, Romano LC, O'Doherty RM, McTiernan CF, O'Donnell CP (2011) Cardiac-specific leptin receptor deletion exacerbates ischaemic heart failure in mice. Cardiovasc Res 89:60–71. https://doi.org/10.1093/cvr/cvq288

34. Narumi T, Watanabe T, Kadowaki S et al (2014) Impact of serum omentin-1 levels on cardiac prognosis in patients with heart failure. Cardiovasc Diabetol 13:84. https://doi.org/10.1186/1475-2840-13-84

35. Huang Y, Lin Y, Zhang S et al (2016) Circulating Omentin-1 levels are decreased in dilated cardiomyopathy patients with overt heart failure. Dis Markers 2016:6762825. https://doi.org/10.1155/2016/6762825

36. Yildiz SS, Sahin I, Cetinkal G et al (2018) Usefulness of serum omentin-1 levels for the prediction of adverse cardiac events in patients with hypertrophic cardiomyopathy. Med Princ Pract 27:107–114. https://doi.org/10.1159/000487396

37. Matsuo K, Shibata R, Ohashi K et al (2015) Omentin functions to attenuate cardiac hypertrophic response. J Mol Cell Cardiol 79:195–202. https://doi.org/10.1016/j.yjmcc.2014.11.019

38. Kataoka Y, Shibata R, Ohashi K et al (2014) Omentin prevents myocardial ischemic injury through AMP-activated protein kinase- and Akt-dependent mechanisms. J Am Coll Cardiol 63:2722–2733. https://doi.org/10.1016/j.jacc.2014.03.032

39. Cardoso-Moreira M, Halbert J, Valloton D et al (2019) Gene expression across mammalian organ development. Nature 571:505–509. https://doi.org/10.1038/s41586-019-1338-5

40. Rao SS, Hu Y, Xie PL et al (2018) Omentin-1 prevents inflammation-induced osteoporosis by downregulating the pro-inflammatory cytokines. Bone Res 6:9. https://doi.org/10.1038/s41413-018-0012-0

41. Li J, Zhu D, Hu S, Nie Y (2022) CRISPR-CasRx knock-in mice for RNA degradation. Sci China Life Sci 65:2248–2256. https://doi.org/10.1007/s11427-021-2059-5

42. Li Y, Li H, Pei J, Hu S, Nie Y (2021) Transplantation of murine neonatal cardiac macrophage improves adult cardiac repair. Cell Mol Immunol 18:492–494. https://doi.org/10.1038/s41423-020-0371-5

43. Ackers-Johnson M, Li PY, Holmes AP, O'Brien SM, Pavlovic D, Foo RS (2016) A simplified, langendorff-free method for concomitant isolation of viable cardiac myocytes and nonmyocytes from the adult mouse heart. Circ Res 119:909–920. https://doi.org/10.1161/CIRCRESAHA.116.309202

44. Yue Z, Chen J, Lian H et al (2019) PDGFR-beta signaling regulates cardiomyocyte proliferation and myocardial regeneration. Cell Rep 28:966–978. https://doi.org/10.1016/j.celrep.2019.06.065

45. Li H, Liu C, Bao M, Liu W, Nie Y, Lian H, Hu S (2020) Optimized Langendorff perfusion system for cardiomyocyte isolation in adult mouse heart. J Cell Mol Med 24:14619–14625. https://doi.org/10.1111/jcmm.15773

46. Feng J, Li Y, Nie Y (2022) Methods of mouse cardiomyocyte isolation from postnatal heart. J Mol Cell Cardiol 168:35–43. https://doi.org/10.1016/j.yjmcc.2022.04.007

47. Karakikes I, Senyei GD, Hansen J et al (2014) Small molecule-mediated directed differentiation of human embryonic stem cells toward ventricular cardiomyocytes. Stem Cells Transl Med 3:18–31. https://doi.org/10.5966/sctm.2013-0110

48. Burridge PW, Matsa E, Shukla P et al (2014) Chemically defined generation of human cardiomyocytes. Nat Methods 11:855–860. https://doi.org/10.1038/nmeth.2999

49. Huang C, Ding T, Zhang Y et al (2023) The longevity protein p66Shc is required for neonatal heart regeneration. J Mol Cell Cardiol 177:21–27. https://doi.org/10.1016/j.yjmcc.2023.02.004

50. Chu Q, Jiang H, Zhang L et al (2020) CACCT: an automated tool of detecting complicated cardiac malformations in mouse models. Adv Sci (Weinh) 7:1903592. https://doi.org/10.1002/advs.201903592

51. Bodis K, Jelenik T, Lundbom J et al (2020) Expansion and impaired mitochondrial efficiency of deep subcutaneous adipose tissue in recent-onset type 2 diabetes. J Clin Endocrinol Metab 105:e1331-1343. https://doi.org/10.1210/clinem/dgz267

52. Phielix E, Jelenik T, Nowotny P, Szendroedi J, Roden M (2014) Reduction of non-esterified fatty acids improves insulin sensitivity and lowers oxidative stress, but fails to restore oxidative capacity in type 2 diabetes: a randomised clinical trial. Diabetologia 57:572–581. https://doi.org/10.1007/s00125-013-3127-2

53. Merino D, Villar AV, Garcia R et al (2016) BMP-7 attenuates left ventricular remodelling under pressure overload and facilitates reverse remodelling and functional recovery. Cardiovasc Res 110:331–345. https://doi.org/10.1093/cvr/cvw076

54. Au-Yeung CL, Yeung TL, Achreja A et al (2020) ITLN1 modulates invasive potential and metabolic reprogramming of ovarian cancer cells in omental microenvironment. Nat Commun 11:3546. https://doi.org/10.1038/s41467-020-17383-2

55. Huang Z, Sun D, Hu JX et al (2016) Neogenin promotes BMP2 activation of YAP and Smad1 and enhances astrocytic differentiation in developing mouse neocortex. J Neurosci 36:5833–5849. https://doi.org/10.1523/JNEUROSCI.4487-15.2016

56. Menzel J, di Giuseppe R, Biemann R et al (2017) Association between chemerin, omentin-1 and risk of heart failure in the population-based EPIC-Potsdam study. Sci Rep 7:14171. https://doi.org/10.1038/s41598-017-14518-2

57. Sam F, Duhaney TA, Sato K et al (2010) Adiponectin deficiency, diastolic dysfunction, and diastolic heart failure. Endocrinology 151:322–331. https://doi.org/10.1210/en.2009-0806

58. Kubin T, Poling J, Kostin S et al (2011) Oncostatin M is a major mediator of cardiomyocyte dedifferentiation and remodeling. Cell Stem Cell 9:420–432. https://doi.org/10.1016/j.stem.2011.08.013

59. Talman V, Teppo J, Poho P et al (2018) Molecular atlas of postnatal mouse heart development. J Am Heart Assoc 7:e010378. https://doi.org/10.1161/JAHA.118.010378

60. Uosaki H, Cahan P, Lee DI et al (2015) Transcriptional landscape of cardiomyocyte maturation. Cell Rep 13:1705–1716. https://doi.org/10.1016/j.celrep.2015.10.032

61. Carrion M, Frommer KW, Perez-Garcia S, Muller-Ladner U, Gomariz RP, Neumann E (2019) The adipokine network in rheumatic joint diseases. Int J Mol Sci 20:4091. https://doi.org/10.3390/ijms20174091

62. Liu H, Wu J, Wang H, Sheng L, Tang N, Li Y, Hao T (2015) Association of serum omentin-1 concentrations with the presence and severity of preeclampsia. Ann Clin Biochem 52:245–250. https://doi.org/10.1177/0004563214541247

63. Tahmasebpour N, Hosseinpour Feizi MA, Ziamajidi N, Pouladi N, Montazeri V, Farhadian M, Abbasalipourkabir R (2020) Association of Omentin-1 with oxidative stress and clinical significances in patients with breast cancer. Adv Pharm Bull 10:106–113. https://doi.org/10.15171/apb.2020.013

64. Tan BK, Adya R, Farhatullah S, Lewandowski KC, O'Hare P, Lehnert H, Randeva HS (2008) Omentin-1, a novel adipokine, is decreased in overweight insulin-resistant women with polycystic ovary syndrome: ex vivo and in vivo regulation of omentin-1 by insulin and glucose. Diabetes 57:801–808. https://doi.org/10.2337/db07-0990

65. Wang Q, Feng X, Zhou C, Li P, Kang J (2013) Decreased levels of serum omentin-1 in patients with obstructive sleep apnoea syndrome. Ann Clin Biochem 50:230–235. https://doi.org/10.1177/0004563212473275

66. Zhou JY, Chan L, Zhou SW (2014) Omentin: linking metabolic syndrome and cardiovascular disease. Curr Vasc Pharmacol 12:136–143. https://doi.org/10.2174/15701611129991402170 95038

67. Çimen AR, Cerit ET, Iyidir OT et al (2017) Serum omentin-1 levels and endothelial dysfunction in obesity. Acta Endocrinol (Buchar) 13:138–143. https://doi.org/10.4183/aeb.2017.138

68. Zengi S, Zengi O, Kirankaya A, Kucuk SH, Kutanis EE, Yigit O (2019) Serum omentin-1 levels in obese children. J Pediatr Endocrinol Metab 32:247–251. https://doi.org/10.1515/jpem-2018-0231

69. Zhang Q, Zhu L, Zheng M et al (2014) Changes of serum omentin-1 levels in normal subjects, type 2 diabetes and type 2 diabetes with overweight and obesity in Chinese adults. Ann Endocrinol (Paris) 75:171–175. https://doi.org/10.1016/j.ando.2014.04.013

70. Rothermel J, Lass N, Barth A, Reinehr T (2020) Link between omentin-1, obesity and insulin resistance in children: Findings from a longitudinal intervention study. Pediatr Obes 15:e12605. https://doi.org/10.1111/ijpo.12605

71. Yang HY, Ma Y, Lu XH et al (2015) The correlation of plasma omentin-1 with insulin resistance in non-obese polycystic ovary syndrome. Ann Endocrinol (Paris) 76:620–627. https://doi.org/10.1016/j.ando.2015.08.002

72. Watanabe K, Watanabe R, Konii H et al (2016) Counteractive effects of omentin-1 against atherogenesis†. Cardiovasc Res 110:118–128. https://doi.org/10.1093/cvr/cvw016

73. Menzel J, Di Giuseppe R, Biemann R et al (2016) Association between omentin-1, adiponectin and bone health under consideration of osteoprotegerin as possible mediator. J Endocrinol Invest 39:1347–1355. https://doi.org/10.1007/s40618-016-0544-3

74. Yin J, Hou P, Wu Z, Nie Y (2015) Decreased levels of serum omentin-1 in patients with inflammatory bowel disease. Med Sci Monit 21:118–122. https://doi.org/10.1265/msm.892081

75. Jin Z, Xia F, Dong J et al (2021) Omentin-1 attenuates glucocorticoid-induced cardiac injury by phosphorylating GSK3β. J Mol Endocrinol 66:273–283. https://doi.org/10.1530/jme-20-0236

76. Zhou JP, Tong XY, Zhu LP et al (2017) Plasma Omentin-1 level as a predictor of good coronary collateral circulation. J Atheroscler Thromb 24:940–948. https://doi.org/10.5551/jat.37440

77. Ji H, Wan L, Zhang Q, Chen M, Zhao X (2019) The effect of omentin-1 on the proliferation and apoptosis of colon cancer stem cells and the potential mechanism. J buon 24:91–98

78. Li D, Mei H, Pu J et al (2015) Intelectin 1 suppresses the growth, invasion and metastasis of neuroblastoma cells through up-regulation of N-myc downstream regulated gene 2. Mol Cancer 14:47. https://doi.org/10.1186/s12943-015-0320-6

79. Li D, Zhao X, Xiao Y et al (2015) Intelectin 1 suppresses tumor progression and is associated with improved survival in gastric cancer. Oncotarget 6:16168–16182. https://doi.org/10.18632/oncotarget.3753

80. Zhang YY, Zhou LM (2013) Omentin-1, a new adipokine, promotes apoptosis through regulating Sirt1-dependent p53 deacetylation in hepatocellular carcinoma cells. Eur J Pharmacol 698:137–144. https://doi.org/10.1016/j.ejphar.2012.11.016

81. Kazama K, Okada M, Yamawaki H (2014) A novel adipocytokine, omentin, inhibits platelet-derived growth factor-BB-induced vascular smooth muscle cell migration through antioxidative mechanism. Am J Physiol Heart Circ Physiol 306:H1714-1719. https://doi.org/10.1152/ajpheart.00048.2014

82. Zhao LR, Du YJ, Chen L et al (2015) Omentin-1 promotes the growth of neural stem cells via activation of Akt signaling. Mol Med Rep 11:1859–1864. https://doi.org/10.3892/mmr.2014.2937

83. Yin L, Huang D, Liu X, Wang Y, Liu J, Liu F, Yu B (2017) Omentin-1 effects on mesenchymal stem cells: proliferation, apoptosis, and angiogenesis in vitro. Stem Cell Res Ther 8:224. https://doi.org/10.1186/s13287-017-0676-1

84. Cabral VLF, Wang F, Peng X et al (2022) Omentin-1 promoted proliferation and ameliorated inflammation, apoptosis, and degeneration in human nucleus pulposus cells. Arch Gerontol Geriatr 102:104748. https://doi.org/10.1016/j.archger.2022.104748

85. Wu SS, Liang QH, Liu Y, Cui RR, Yuan LQ, Liao EY (2013) Omentin-1 stimulates human osteoblast proliferation through PI3K/Akt signal pathway. Int J Endocrinol 2013:368970. https://doi.org/10.1155/2013/368970

86. Yang RZ, Lee MJ, Hu H et al (2006) Identification of omentin as a novel depot-specific adipokine in human adipose tissue: possible role in modulating insulin action. Am J Physiol Endocrinol Metab 290:E1253-1261. https://doi.org/10.1152/ajpendo.00572.2004

87. de Souza Batista CM, Yang RZ, Lee MJ et al (2007) Omentin plasma levels and gene expression are decreased in obesity. Diabetes 56:1655–1661. https://doi.org/10.2337/db06-1506

88. Jialal I, Devaraj S, Kaur H, Adams-Huet B, Bremer AA (2013) Increased chemerin and decreased omentin-1 in both adipose tissue and plasma in nascent metabolic syndrome. J Clin Endocrinol Metab 98:E514-517. https://doi.org/10.1210/jc.2012-3673

89. Pan HY, Guo L, Li Q (2010) Changes of serum omentin-1 levels in normal subjects and in patients with impaired glucose regulation and with newly diagnosed and untreated type 2 diabetes. Diabetes Res Clin Pract 88:29–33. https://doi.org/10.1016/j.diabres.2010.01.013

90. Auguet T, Quintero Y, Riesco D et al (2011) New adipokines vaspin and omentin. circulating levels and gene expression in adipose tissue from morbidly obese women. BMC Med Genet 12:60. https://doi.org/10.1186/1471-2350-12-60

91. Li Z, Zhang Y, Tian F, Wang Z, Song H, Chen H, Wu B (2020) Omentin-1 promotes mitochondrial biogenesis via PGC1α-AMPK pathway in chondrocytes. Arch Physiol Biochem. https://doi.org/10.1080/13813455.2020.1819337

92. Groppe J, Greenwald J, Wiater E et al (2002) Structural basis of BMP signalling inhibition by the cystine knot protein Noggin. Nature 420:636–642. https://doi.org/10.1038/nature01245

93. Rebbapragada A, Benchabane H, Wrana JL, Celeste AJ, Attisano L (2003) Myostatin signals through a transforming growth factor beta-like signaling pathway to block adipogenesis. Mol Cell Biol 23:7230–7242. https://doi.org/10.1128/MCB.23.20.7230-7242.2003

94. Cao Y, Wang Y, Zhou Z et al (2022) Liver-heart cross-talk mediated by coagulation factor XI protects against heart failure. Science 377:1399–1406. https://doi.org/10.1126/science.abn0910

95. Dale JK, Vesque C, Lints TJ, Sampath TK, Furley A, Dodd J, Placzek M (1997) Cooperation of BMP7 and SHH in the induction of forebrain ventral midline cells by prechordal mesoderm. Cell 90:257–269. https://doi.org/10.1016/s0092-8674(00)80334-7

96. Luo G, Hofmann C, Bronckers AL, Sohocki M, Bradley A, Karsenty G (1995) BMP-7 is an inducer of nephrogenesis, and is also required for eye development and skeletal patterning. Genes Dev 9:2808–2820. https://doi.org/10.1101/gad.9.22.2808

97. Tseng YH, Kokkotou E, Schulz TJ et al (2008) New role of bone morphogenetic protein 7 in brown adipogenesis and energy expenditure. Nature 454:1000–1004. https://doi.org/10.1038/nature07221

98. Zeisberg EM, Tarnavski O, Zeisberg M et al (2007) Endothelial-to-mesenchymal transition contributes to cardiac fibrosis. Nat Med 13:952–961. https://doi.org/10.1038/nm1613

99. Tan CY, Wong JX, Chan PS et al (2019) Yin Yang 1 suppresses dilated cardiomyopathy and cardiac fibrosis through regulation of

Bmp7 and Ctgf. Circ Res 125:834–846. https://doi.org/10.1161/CIRCRESAHA.119.314794

100. Murphy SA, Miyamoto M, Kervadec A et al (2021) PGC1/PPAR drive cardiomyocyte maturation at single cell level via YAP1 and SF3B2. Nat Commun 12:1648. https://doi.org/10.1038/s41467-021-21957-z